12-2005

Photo-Acoustic Analysis of Dental Materials and Tissue

Pavlina Jetchkova Jeleva
University of Tennessee - Knoxville

To the Graduate Council:

I am submitting herewith a dissertation written by Pavlina Jetchkova Jeleva entitled "Photo-Acoustic Analysis of Dental Materials and Tissue." I have examined the final electronic copy of this dissertation for form and content and recommend that it be accepted in partial fulfillment of the requirements for the degree of Doctor of Philosophy, with a major in Physics.

Christian G. Parigger, Major Professor

We have read this dissertation and recommend its acceptance:

Lloyd M. Davis, James W. L. Lewis, Jack W. Buchanan, Robert Splinter

Accepted for the Council:
Carolyn R. Hodges

Vice Provost and Dean of the Graduate School

(Original signatures are on file with official student records.)

To the Graduate Council:

I am submitting herewith a dissertation written by Pavlina Jetchkova Jeleva entitled "Photo-Acoustic Analysis of Dental Materials and Tissue." I have examined the final electronic copy of this dissertation for form and content and recommend that it be accepted in partial fulfillment of the requirements of the degree of Doctor of Philosophy, with a major in Physics.

Christian G. Parigger
Major Professor

We have read this dissertation
and recommend its acceptance:

Lloyd M. Davis

James W. L. Lewis

Jack W. Buchanan

Robert Splinter

Accepted for the Council:

Anne Mayhew
Vice Chancellor and
Dean of Graduate Studies

(Original signatures are on file with official student records.)

Photo-Acoustic Analysis of Dental Materials and Tissue

A Dissertation
Presented for the
Doctor of Philosophy
Degree
The University of Tennessee, Knoxville

Pavlina Jetchkova Jeleva
December 2005

Dedication

To my son Raymond Alexander.

Acknowledgments

This work would not be possible without the support, the criticism, and the helpful assistance of many people.

First of all, I would like to express my gratitude to Dr. Christian Parigger, who supervised my research with excellent guidance, patience and encouragement.

I would like to thank Dr. Robert Splinter and Dr. Kayvan Najarian from the University of North Carolina at Charlotte for their great insights and advice.

I am thankful to Dr. Peter Lockhart from Carolinas Medical Center for his expertise on the medical aspects of the project.

I also thank Dr. James Lewis and Dr. Lloyd Davis for their valuable support and advice.

Thanks to Dr. Jack Buchanan from the University of Tennessee Health Center for his efforts to establish a collaboration with UTSI for cardiac research.

I am indebted to Newt Wright for his enormous help in the lab.

Finally, I take this opportunity to express my gratitude and love to my husband, my parents and my brother, Kate and David Lansford, and Stephanie Edwards, for their moral support and encouragement.

Abstract

The goal of the presented study is the investigation of the feasibility of using optically generated acoustic waves for analysis of dental material below laser-ablation threshold.

The temperature rise of dental material and tissue has been modeled analytically and numerically, and measured experimentally. Following interactions with nano- and femto-second laser radiation the temperature rises at a rate of typically $1°C$ per J/cm^2, along with the generation of an acoustical wave. The results from the models agree with the experiment. The acoustic measurements show differences in the acoustic signal strength and the frequency spectrum when the canal in the porcelain phantom is empty or filled with intralipid solution.

The photo-acoustic technique is found to be suitable for detection of liquids under a layer of dental porcelain material, consequently it can be the basis for building an imaging tool for dental diagnostic applications. By generating sound waves in the pulp, one would be able to evaluate it's state and the overall health of the tooth. This is of vital importance for diagnosing initial-stage inflammation.

Contents

List of Tables

List of Figures

Chapter 1

Introduction

Dental health plays a major role in the interest of public health. Early detection of dental tissue inflammation can be lifesaving for patients undergoing heart valve replacement surgery, radiotherapy or chemotherapy.

Currently the diagnostic tools available at the conventional dental offices are inadequate to yield sufficient information on the viability of the tooth pulp. The pulp is the core of the tooth and consists mainly of connective tissue, nerves, blood vessels and collagen. Inflammation of dental pulp tissue, which can induce severe pain, originates from a variety of causes, including trauma and dental caries (decay). Dental caries arises from bacterial colonization of the outer densely calcified tooth surface. Bacteria excrete acid, which decalcifies the enamel, creating a hole, which encourages additional bacterial growth. When the caries spreads through the dentin and reaches the pulp, it results in inflammation of the pulp which causes an increased blood flow, i.e., erythema.

When the inflammation reaches a certain level, the process is irreversible - the pulp deteriorates. This will in turn eliminate the blood flow to the tooth. In addition, after it has damaged the pulp, inflammation migrates into the jaw and leads to life threatening conditions. Therefore, a quantitative assessment of the amount of blood in the pulp will offer important information on the status of the tooth health. Early detection of pulp inflammation would allow dentists to diagnose and initiate treatment before the tooth is in irreversible state and well before it threatens the viability of the tooth, and before the patient becomes infected. Unfortunately, at present, this is difficult and in most cases impossible.

The available diagnostic methods for dental applications include magnetic resonance imaging (MRI), computer tomography (CT), and conventional dental radiography. The first two techniques are costly and are mostly used in experimental settings on extracted teeth. Dental radiographs do not produce sufficient spacial resolution and cannot image soft tissue (pulp). In addition, for visualizing blood flow a radio-opaque substance needs to be injected. It is definitely not possible to image underneath artificial crowns using conventional methods.

Therefore, there is a need for a new type of visualization technique, which would give dentists the opportunity to diagnose and initiate treatment before the state of the tooth health is irreversible. Such an innovation in imaging techniques will also lead to a better understanding of the processes leading to these conditions.

The difficulties in the penetration of any kind of radiation are due to the unique

structure of the enamel. It consist of tightly packed hydroxyapatite crystals, which are organized in structures called "rods". The rods are almost cylindrical in shape and are surrounded by crystals oriented in different directions from those making up the rods [1].

Laser photo-acoustic (PA) spectroscopy is a highly sensitive absorption technique used in a variety of applications for detection of small concentrations of molecular species, study of a variety of biochemical reactions, as well as photothermal expansions and contractions of molecules. The advantage of the PA technique is that the signal is generated primarily as a result of the absorption of light. Distortion of the signal due to scattering is not an issue as in other imaging methods. Recently, it has been shown to be viable for variety of biomedical applications, such as visualization of tumor angiogenesis and characterization of arterial walls.

The goal of this work is the development of a cost-effective photo-acoustic imaging method to quantify the amount of blood in the tooth pulp. This will eventually lead to the development of a clinical tool in dentistry to determine tooth health viability.

The purpose of this dissertation is to show that it is possible to detect the presence of blood underneath natural and artificial dental crowns.

Chapter two describes in detail the physiological, optical, acoustical, thermal, and mechanical properties of dental tissue. They are crucial to understanding the processes of energy deposition, sound generation and propagation.

Chapter three gives a few examples of biomedical applications of the photo-acoustic

method.

Chapter four discusses the general theoretical description of optical sound generation.

Sound generation from femto-second laser pulses is considered separately in chapter five to emphasize the difference in the underlying physical processes. The pulses are considered infinitely short and are approximated with a Delta distribution. The results are compared with the experiments.

Chapter six is divided into two parts: nanosecond and femto-second experiments. They include both pressure and temperature measurements. It is shown that there are differences in the spectroscopic signal coming from a porcelain cube whose canal has been filled with intralipid solution vs. a hollow canal.

Discussion and recommendations for further work are given in chapter seven.

Chapter 2

Properties of Dental Tissue

2.1 Basic Anatomy of the Tooth

A tooth consists of a crown, neck and a root. The visible part of the tooth above the gum is called the crown. The roots are embedded in the jaw bone and the neck is constricted between the roots and the crown. The neck and the root are covered to a great extend with a mucous tissue called gingiva. Fig.2.1 [2] illustrates the anatomy of the tooth.

The crown is covered by a layer of the most mineralized tissue known - the enamel. It's thickness varies between 1 and 3 mm and it consists of about 96 vol% hydroxyapatite ($Ca_{10}(PO_4)_6(OH)_2$) crystals, 4 vol% organic material and water.[1] Carious enamel is characterized by decreased mineral content and increased inhomogeneity. The hydroxyapatite crystals (HAC) have variable length up to 10 μm and thickness of 25 to 40 nm. They are organized in cylindrical structures called "rods" with diameter of about

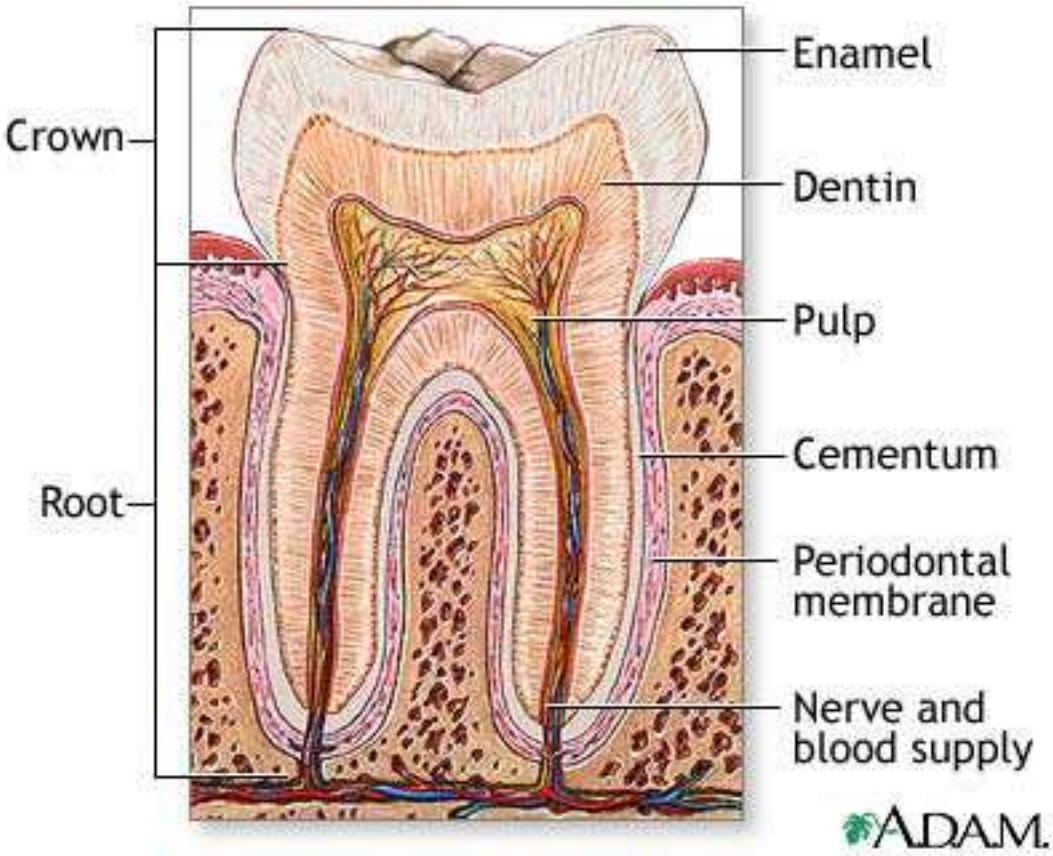

Figure 2.1: Basic anatomy of a tooth

5 μm. For the most part, the axes of the crystals within the rods run parallel to its longitudinal axis. The rods are surrounded by crystals oriented in different directions from those making up the rods.

The bulk of the tooth consists of dentin, which is a bone like tissue and it is less mineralized - about 70 % inorganic, 20% organic material and 10 % water by weight and 45 %, 33%, and 22 % by volume, respectively.[1] The purpose of dentin is to support the extremely fragile enamel.

Fig.2.2 shows the various structures can be distinguished in dentin.[3] Dentinal tubules traverse the entire thickness of the dentin. Their diameter varies, ranging from 900 nm near the dentinoenamel junction (DEJ), 1.2 μm in the middle portion of the dentin to 2.5 μm near the pulp. The density of the tubules is higher at the pulpal surface and ranges from 59,000 to 76,000 per square millimeter. The hypermineralized ring of dentin forming the tubule walls is called peritubular or intratubular dentin. It is approximately 44 nm wide near the pulpal end and 750 nm near the DEJ. The dentinal tubules are surrounded by the intertubular dentin. The intertubular dentin consists of tightly interwoven collagen fibrils and HAC. The fibrils are randomly oriented in a plane at right angles to the dentinal tubules. The tubules clog with HAC with age which causes the dentin to mineralize. The HAC are on average 100 nm long and are oriented with their long axes parallel to the fibril.[1, 4] There is a possibility that density, orientation and distribution of the tubules play role in the mechanical properties of dentin.[5] They play role in the dentin formation as well since they contain the cytoplasmic extensions

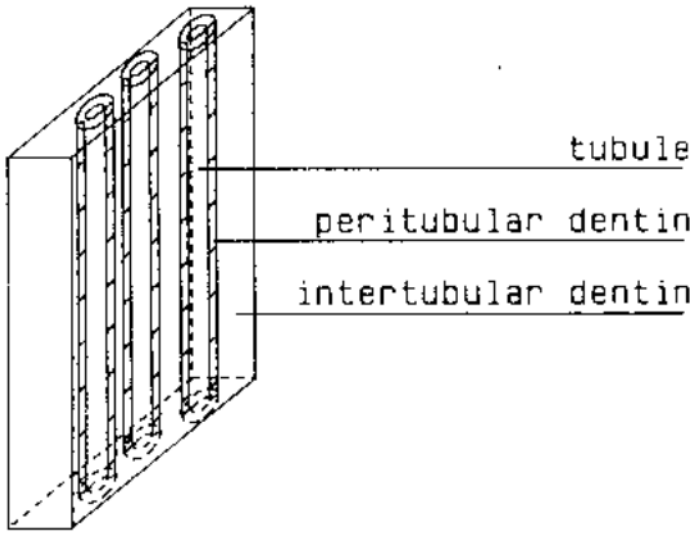

Figure 2.2: Structure of dentin

of the odontoblasts. First, the odontoblastic cells form the dentin and later maintain it when stimulated. This makes the dentin much different than enamel, since it is capable of repair.[1] The pulp is the living tissue of the tooth. It is located in the pulp chamber and root canals. It consists mainly of nerves, connective tissue, collagen, lymph and blood vessels. The pulp is nourished via vessels entering and leaving the root canal at the apical delta and accessory canals originating from the jaw bone.

2.2 Optical Properties of Dentin and Enamel

Investigating the optical properties of dental tissue is important for developing better diagnostic techniques. As the density of the tissue decreases from the enamel to the pulp of the tooth, so does its index of refraction. The optical properties also depend on the

Table 2.1: Refractive index of enamel

Wavelength [nm]	Index of Refraction	Reference
220	1.725	Duplain *et al* [6]
300	1.650	Spitzer & Ten Bosch 1975 [7]
350 - 700	1.625	
9209	0.62	Duplain *et al* [6]
9505	1.05	
9621	1.48	
10171	2.43	
10765	1.93	

orientation of the crystalline structures. Table 2.1 the refractive index of dental enamel in the far infrared region as it was investigated by Duplain *et al*[6] using a reflectance measurement method. They reported a strong wavelength dependence of the optical properties in the region of the absorption band of hydroxyapatite. The real part of the refractive index increased from 0.62 at 9.209 μm to 2.43 at 10.632 μm and then decreased again to 1.93 at 10.765 μm. Transmission and reflectance measurements of thin slabs of enamel performed by Spitzer and Ten Bosch showed that in the visible spectrum the refractive index of the enamel is 1.73 at 220 nm and 1.62 for wavelengths between 400 and 700 nm [7] (Table 2.1). Table 2.2 shows the calculated refractive indices of different structures in dentine according to their composition as given by Zijp and Ten Bosch.[3] Based on the mineral content and the volume they estimated the refractive index of whole dentine to be 1.49. The peritubular dentin, being more mineralized has an index of 1.59, which is quite different from the 1.45 value for the intertubular dentin. It was assumed that the tubules were filled with water.

Table 2.2: Composition of dentin (Vol. %)and resulting refractive indices

Compartment	Mineral	Collagen	Noncolagenous Proteins	Water	Refractive Index
Whole dentine	48	25.5	2.5	24	1.49
Tubules	0	0	0	16	1.33
Bulk Dentin	48	25.5	2.5	8	1.52
Peritubular	25.7	0	0.6	2.3	1.59
Intertubular	22.3	25.5	1.9	5.7	1.45
Intrafibrilllar	21.2	25.5	0	3.2	1.49
Interfibrillar	1.1	0	1.9	2.6	1.41
Refractive index	1.62	1.4	1.4	1.33	

The optical absorption and scattering of dental enamel has been investigated by many authors theoretically and experimentally, but they do not seem to agree. Spitzer and ten Bosch (1975) [7] measured the diffuse transmission and reflection values of thin tissue slabs in an integrated sphere in the UV and visible spectrum. Using the Kubelka-Munk theory they calculated the absorption μ_a and scattering μ_s coefficients. They found an absorption peak of 12.2 cm^{-1} at 220 nm, after which there was steady decrease to 1.7 cm^{-1} at 400 nm, 0.7 cm^{-1} at 550 nm and about 0.6 cm^{-1} at 700 nm. From the same authors the values of the scattering coefficients at the respective wavelengths were given as follows. 380 cm^{-1}, 230 cm^{-1}, 93 cm^{-1}, 40 cm^{-1}, and 12 cm^{-1} respectively. Nicolaides obtained 0.1 cm^{-1} for the absorption coefficient at 488 nm and a range of values from 92 to 400 cm^{-1} for the scattering coefficient.[8] Groenhuis's values for the scattering coefficient are 45 cm^{-1} at 500 nm, 33 cm^{-1} at 600 nm and 27 cm^{-1} at 700 nm [9]. Fried *et al* [10] measured the scattering properties of enamel and dentin sections of variable thicknesses at 543 nm, 632 nm and 1053 nm. It was found that the

absorption coefficients of the enamel are negligible, while the scattering coefficients were 105 cm^{-1} at 543 nm, 60 cm^{-1} at 632 nm, and only 15 cm^{-1} at 1053 nm. By measuring the scattering intensity functions of He-Ne laser (633 nm) light of 80 to 100 μm thick human enamel, Zijp *et al* [11] found the scattering coefficient to be 66 cm^{-1}.

Spitzer and ten Bosch (1975) [7] gave values for the dentin scattering 45 cm^{-1} at 543 nm and 25 cm^{-1} at 632 nm. The absorption coefficients were less than 1 cm^{-1} for both wavelengths. Ten Bosch and Zijp [12] measured the scattering and absorption coefficients for 170 μm thick dentin slices. The absorption coefficient of 4 cm^{-1} was found not to be very dependent on the wavelength. At the center of the coronal dentin the values for the scattering coefficient were 30 cm^{-1} and 80 cm^{-1}. The scattering coefficient was found to be slowly decreasing with the wavelength and hardly related to the mineral content. Later the same authors measured he scattering phase functions for He-Ne laser light of 10-20 μm thick slabs and the value for the scattering coefficient was found to be 1200 cm^{-1}, much larger than before. Their theoretical model [3] predicted a value of 190 cm^{-1}, much smaller than the measured 1200 cm^{-1} for randomly oriented collagen fibers. However, the single-cylinder theory gave a much closer value of 1400 cm^{-1}. Nicolaides [8] measured scattering of 122 cm^{-1} and absorption of 0.1 cm^{-1}. Tables 2.3 and 2.4 present a summary of published optical properties of enamel and dentin, respectively.

Table 2.3: Optical absorption and scattering coefficients of dental enamel

Wavelength nm	μ_a cm^{-1}	μ_s cm^{-1}	Reference
220	12.2	380	Spitzer & Ten Bosch 1975 [7]
300	7.5	230	
400	1.7	93	
488	0.1	300	Nicolaides *etal* 2002 [8]
500	1.16	58	Spitzer & Ten Bosch 1975 [7]
543	<1	105	Fried *etal* 1995 [10]
550	0.8	40	Spitzer & Ten Bosch 1975 [7]
632	<1	60	Fried *etal* 1995 [10]
632	0.6	25	Spitzer & Ten Bosch 1975 [7]
700	0.6	23	
1053	<1	15	Fried *etal* 1995 [10]

Table 2.4: Optical absorption and scattering coefficients of dentin

Wavelength nm	μ_a cm^{-1}	μ_s cm^{-1}	Reference
488	0.1	122	Nicolaides *etal* 2002 [8]
535	4	30	Ten Bosch and Zijp 1987 [12]
543	3-4	280	Fried *etal* 1995 [10]
550	4	30	Ten Bosch and Zijp 1987 [12]
632	3-4	280	Fried *etal* 1995 [10]
632	6	1200	Zijp and Ten Bosch 1991 [13]
1053	3-4	15	Fried *etal* 1995 [10]

2.3 Acoustic Properties

Ultrasound has been used widely for medical imaging and for non-destructive evaluation of materials because of its ability to detect physical discontinuities, such as fractures or cracks. Several authors have demonstrated the feasibility of this technology for dental imaging. The first to estimate the enamel and dentin thickness on extracted teeth were Barber and Lees [14] in 1969. However, to properly couple the transducer they needed to grind a flat surface on the tooth. In another significant theoretical and experimental study Ghorayeb *et al* [15] reported coupling a PZT transducer to extracted human tooth immersed in water. They were clearly able to distinguish the dentino-enamel junction (DEJ) and the boundary of the pulp. In their study they used 6200 m/s for the sound velocity in enamel and impedance of 18.75 MRayls. The velocity in dentin was smaller - 3800 m/s and the impedance was 7.6 MRayls. Pulp was considered to have properties close to those of water and the velocity was taken 1570 m/s with 1.57 MRayls impedance. Most recently Culjat *et al* [16] presented a B-scan around the circumference of an extracted human tooth, immersed in water, which showed a complete image of the outer enamel surface and the DEJ. The author used 5700 m/s for the velocity and 16.92 MRayl impedance value. Although the velocities of sound in both dentin and pulp appear to be similar as the ones given by Ghorayeb, i. e., 3800 m/s and 1540 m/s, respectively, the impedances are different because of differences in the values of the density that were used. Table 2.5 shows the acoustic properties of dental tissue given in the literature. Using acoustic microscopy measurements Maev *et al* [17] measured

Table 2.5: Acoustic properties of dental tissue

Tissue	Mass Density kg/m^3	Sound Velocity m/s	Impedance MRayls	Reference
Enamel	3000	6250	18.75	Ghorayeb & Valle 2002 [15]
	2970	5700	16.92	Culjat *etal* 2003 [16]
		5900		Maev *etal* 2002 [17]
White spot carious enamel		4900		
Enamel in area of carious cavity		5500		
Dentin	2000	3800	7.6	Ghorayeb & Valle 2002 [15]
	2140	3800	8.13	Culjat *etal* 2003 [16]
		3770		Maev *etal* 2002 [17]
Dark dentin near enamel		3490		
Dark dentin near pulp		3240		
Transparent dentin		4500		
Dentin in area of carious cavity		3600		
Pulp	1000	1570	1.57	Ghorayeb & Valle 2002 [15]
	1060	1540	1.6	Culjat *etal* 2003 [16]
Cementum		3300		Kossoff and Sharpe 1966

the longitudinal sound velocity in flat-parallel sections of human premolars. The TOF measurements performed in sound and carious areas showed differences in the velocities due to the different impedances in these areas. For example, in areas of healthy dark dentin tissue near the pulp sound has lower velocity than in areas of dark dentin near the enamel. Also, the velocity tends to lower in areas of carious enamel withe respect to sound enamel (see Table 2.5).

2.4 Mechanical Properties

Restorative procedures are essential in dental practices. Knowledge of the mechanical properties of enamel and dentin is important for the development of quality restorative materials. The elastic modulus of the material must be compatible with the one in the

Table 2.6: Elastic modulus (E) and hardness (H) of dental tissue

Tissue	Comments	E [GPa]	H [GPa]	Reference
Whole tooth	premolar	24.0		Povolo & Hermida 2000 [19]
	canine	46.2		
Enamel	parallel to rods	87.5	3.8	Habelitz *et al* 2001 [20]
	perpendicular to rods	72.7	3.3	
	rod's head	88.0	4.3	
	rod's tail	80.3	3.7	
	enamel surface	91.1	4.6	Cuy *et al* 2002 [21]
	EDJ	66.2	3.4	
		90.59	3.4	Willems *et al* 1993 [22]
	occlusal direction	125.0		Lees & Rollins 1972 [23]
	longitudinal direction	115.0		
	occlusal direction	98.0	3.7	Xu *et al* 1998 [24]
	longitudinal direction	86.0	3.1	
Dentin	dry isotropic	28.3		Kinney *et al* 2004 [25]
	wet isotropic	24.4		
	dry hexagonal	E_{11}=28.1		
		E_{33}=27.6		
	wet hexagonal	E_{11}=25.0		
		E_{33}=23.2		
	pulp wall	11.59	0.52	Angker *et al* 2003 [26]
	middle area	17.06	0.85	
	EDJ	16.33	0.91	

original tooth. Differences in the mechanical properties are also indicative for the health state of the tooth. Due to the difficulties in making accurate mechanical tests on small specimens, there are some discrepancies in the reported values of the Young's modulus. Table 2.6 shows a summary of the values of the elastic modulus and the hardness of dental tissue as given in the literature. A detailed literature review of published research on mechanical properties of human dentin was given by Kinney *et al.*[18]

Povolo and Hermida [19] measured the mean elastic moduli of premolar and whole canine teeth using high frequency piezoelectric excitation and compared the results with

those obtained by indentation techniques. They reported values of 24 GPa and 46.2 GPa for non-carious premolar and canine respectively. Non-indentation techniques of the same samples determined values of the elastic moduli of 95 GPa for enamel and 12 GPa for dentin.[27] Cuy *et al* [21] mapped the hardness and the elastic modulus of a maxillary second molar. The results indicated a spatial variation of the mechanical properties. Both the hardness and the elastic modulus decreased from 4.6 to 3.4 GPa and from 91.1 to 66.2 GPa, respectively when going from the enamel surface to the enamel-dentine junction. Such variations have been detected in the past and they have been attributed to the degree of tissue mineralization. It is important to mention here that the degree of mineralization depends on the age and medical history of the individual. For example, Staines *et al* [28] reported 3 GPa change in the elastic modulus for 1 vol. % change in the HAP content. Using atomic force microscope combined with a nano-indentation technique Habelitz *et al* [20] found that the elasticity and hardness were also a function of the microstructural texture. The measurements on human third molars showed mean Young's moduli of 87.5 and 72.7 GPa and hardness of 3.9 and 3.3 GPa in parallel and perpendicular directions to the enamel rods, respectively. Spears [29] constructed a finite element model of the elastic modulus. The calculation showed that the Youngs modulus varied from 93 to 113 GPa when the crystalline fraction changes from 0.81 to 0.99 in direction parallel to crystal orientation and from 19 to 91 GPa in perpendicular direction. Spatial variation was also reported after measurements at different locations on single enamel rods. These results showed decrease in the Young's modulus from 88

to 80.3 GPa at the head and tail areas, respectively. The hardness value decreased as well from 4.3 to 3.7 GPa at the head and tail areas, respectively.

Because of the lower mineral content in dentin one expects that the elastic modulus will have a lower value than that of enamel. In an extensive review of research published in the last 50 years, Kinney *et al* [18] reported a large variation in the magnitude of the Young's modulus. A comparison between sonic and indentation measurements lead him to believe that the value of the elastic modulus lies between 18 and 25 GPa. As in enamel the elastic properties of dentin are anisotropic. Using resonant ultrasound spectroscopy a year later Kinney *et al* [25] measured the second order elastic properties of dry and hydrated human dentin. The Young's modulus for isotropic dry and wet dentin was reported o be 28.3 and 24.4 GPa. In perpendicular direction to the tubuli if hexagonal symmetry of dry and wet dentin was considered the measured values were 28.1 and 25.0 GPa, respectively. The same parameters, but for direction along the tubule axis, the values are 27.6 and 23.2 GPa. Angker *et al* [26] investigated the spatial variation of the mechanical properties of dentin using the indentation technique. The results show that both the hardness and the elastic modulus decrease towards the pulp wall. Near the DEJ the hardness and the Young's modulus have values of 0.91 and 16.33 GPa, respectively. The same parameters were 0.85 and 17.06 GPa in the middle area and 0.52 and 11.59 GPa towards the pulp wall.

The mechanical properties of dental tissue reflect their complex structure. Both enamel and dentin are anisotropic and inhomogeneous. Their elasticity and hardness

tend to decrease towards the pulp. Such changes are correlated to the the mineral content and histological structure of tissue.

Chapter 3

Applications of Photo-Acoustics for Medical Imaging

Noninvasive methods for imaging biological tissue are essential for quality health care. A significant amount of work has been dedicated in the past years for developing optical diagnostic techniques to eliminate the use of ionizing radiation, as well as the use of radioactive sources. The challenge is in the turbid nature of biological tissue, which causes the light to scatter multiple times and the information to be lost. This has been overcome by the use of both time-resolved acoustical and optical signal detection.

3.1 Photo-Acoustic Spectroscopy

Laser photo-acoustic spectroscopy is a technique in which information about the specimen is carried in the acoustic signal produced as a result of the absorption of laser light

and the subsequent expansion of the heated volume. Recently it has been developed to a point where visualization of structures in biological tissue seems to be an attainable technology. A photo-acoustic tomographic technique for visualizing the angiogenesis around tumors was developed by Hoelen *etal* reaching resolution of $10\mu m$.[30] Using time-resolved photo-acoustic measurements Beard *etal*. characterized both the chemical composition and the thickness of arterial wall. The photo-acoustic imaging method is based on the optical absorption differences in the tissue microstructures. When light propagates in any medium, it is scattered and absorbed. The absorption of the energy causes the temperature to rise slightly. When the heating stops the tissue will cool and relax, resulting in a damped harmonic oscillation. The pressure wave generated in this process is detected by means of piezoelectric devices. An image is generated by combining the signal of any number of detectors by interpolation of time-of-flight measurements. By analyzing the frequency content in the signal the properties of the material can be revealed based on the resonance frequencies for the respective Young's moduli. For high resolution applications, where the frequency of the generated wave is tens of MHz, a wide band detection sensitivity is required. Recently, hydrophones made of the ferroelectric and pyroelectric polymer poly(vinylidene fluoride) (PVDF) have become very popular for medical imaging applications. Their frequency response ranges from 0 to 60 MHz with a maximum response at about 30 MHz. Another advantage of PVDF detectors is that when arranged into detector arrays their performance is much better than piezoelectric transducer arrays.

3.2 Visualizing Tumor Angiogenesis

Tumor development is directly correlated to increased vascularization of the diseased tissue. Pulsed photo-acoustic (PA) technique was shown to be a sensitive tool for the early detection of tumor formation via determination of blood concentrations in turbid media. Hoelen *et al* [30, 31] performed series of experiments to develop a Photoacoustic Tissue Scanning technique (PTS) to detect blood vessels in tissue. The PA signals were generated by a 8 ns light pulses at 532 nm and pulse energies of 70-80 μJ. Human hairs and artificial capillaries filled with whole blood and Evans blue solutions were used for the absorption studies. These were dipped in 10 % solution of Intralipid or incorporated in chicken breast. Figure 3.1 shows the experimental set up for photo-acoustic scanning of absorbers in turbid media. A glass fiber illuminates the sample and a PVDF film transducer of 200 μm diameter detects the acoustic signal .[30] Figure 3.2 illustrates the result obtained by detecting only signals originating from the front and the back sides of the capillary.[30] The signals seem to be faster in tissue. A depth resolution of 10 μm was achieved, as well as a lateral resolution of 200 μm limited by the diameter of the transducer. The image was retrieved by taking into account the signal from each detector in the array as a function of acoustical time-of-flight. According to the authors, the same resolution could be obtained by using Optical Coherence Tomography, but only for 1 mm depth, while PA can be used for measurements for a depth of 1 to 10 mm.

The laser optoacoustic imaging system (LOIS) for breast cancer detection developed by Oraevski *et al* [32]. They showed the capability of the system to detect small volumes

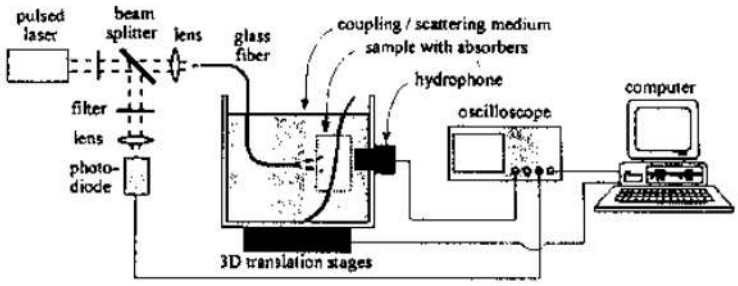

Figure 3.1: PA detection of absorbers in turbid media

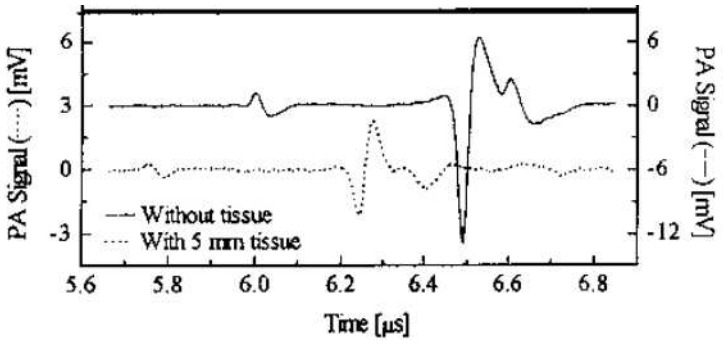

Figure 3.2: PA signals generated by capillary flow of Evans Blue solution

up to 6 cm depth in the tissue. A compact Nd:YAG laser system delivers 10 ns pulses via a fiberoptic light delivery system. The data acquisition system consists of a linear array of 12 wide band acoustic transducers and a computer with a custom made signal processing and image reconstruction code. The opto-acoustic contrast achieved a value of 300 % between the tumor and the breast tissue. The experiments were performed on phantoms, as well as breast samples. The tumor phantom was made of optically turbid gel colored with bovine hemoglobin and a spherical (8 mm diameter) tumor-like component with absorption coefficient of 0.75 cm^{-1}. Also an acoustically homogeneous and radiologically dense breast phantom was made for this study. The same group designed an opto-acoustic tomography technique for imaging of oral cancer [33]. The resolution they achieved was 15x30 μm up to a depth of 5 mm. The advantage of the new method is based on the development of the Opto-Acoustic Front Surface Transducer. The schematic of the transducer is given in Fig.3.3.[33] "Laser pulses were delivered to the opto-acoustic prism (1) of the transducer via an optical fiber (2), focused by a condenser (3) onto the surface of tissue under investigation (4). The generated ultrasonic waves emitted into a transparent opto-acoustic prism made of quartz are detected with a wide-band LiNbO3 piezoelectric transducer (5)".[33]

3.3 Characterization of Blood Vessels

Recently, Beard P. C. and Mills T. N. [34, 35] elaborated that time-resolved PA imaging has a great potential for characterizing normal and atheromatous arterial tissue. This

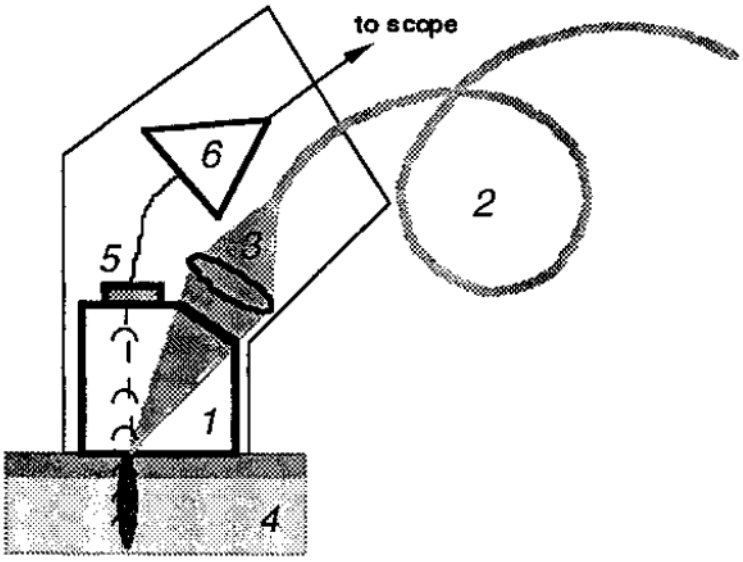

Figure 3.3: Opto-Acoustic Front Surface Transducer

technique is capable of producing both composition and thickness information of the vessel wall. Nanosecond laser pulses at 436, 461, and 532 nm were used to generate thermoelastic waves in different media. The reflected waves were detected with the help of a PVDF membrane hydrophone after they were reflected from a glass block. Figure 3.4 illustrates the setup for their experiment.[34] The incident fluence was 0.17 mJ mm^{-1} and the pulse duration 13 ns. The measurements show that the shape and the amplitude of the waves were consistent for different points on the aorta specimen. In some cases signals coming from different specimen would show the presence of a second peak in the initial part of the wave. The authors believe that this is due to the generation of a second thermoelastic wave at the intima-media boundary. To visualize blood vessels *in vivo* Kolkman *et al* [36] applied photo-acoustics using NIR light from a Q-switched Nd:YAG laser with 10 ns pulses at a repetition rate of 10 Hz. The light

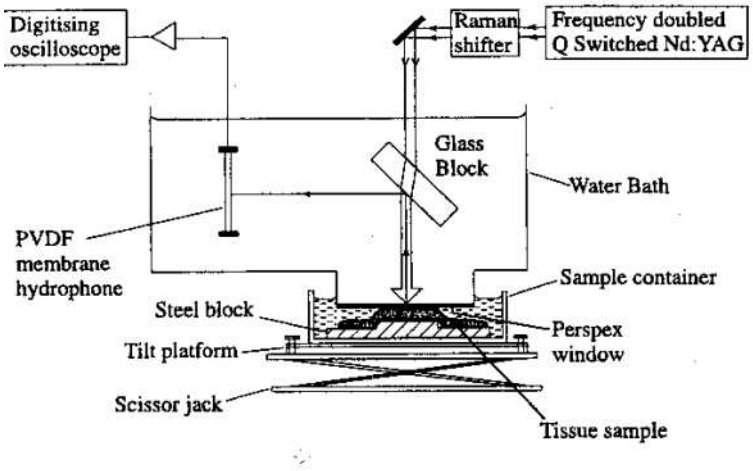

Figure 3.4: PA detection of absorbers in turbid media

is delivered via a glass fiber, which was embedded in the center of the photo-acoustic sensor. The authors performed nine linear scans with 31 measurements on each line and 1 mm distance between the scans. This provided enough information to construct a 2-D cross-sectional image on each line, which showed the joining of the vessels.

3.4 Depth Imaging of Port-Wine Stains

Knowledge of the depth profile of port-wine stains (PWS) helps the clinicians determine the optimal cooling procedure for the patients. This can be achieved by inducing PA thermoelastic expansion of the target chromophores. Viator *et al* [37] developed a PA probe to determine the epidermal and PWS blood vessel depths. The probe consisted of two 1500 μm diameter optical fibers and a coaxial cable which has a 25 μm thick

PVDF film attached to the end. They were all housed in a water-filled contained to achieve better impedance matching with the target surface. The two fibers delivered light separately, so the total amount of energy delivered to the skin is larger. The results from measurements with tissue phantoms showed discrepancies from 5 % to 13 %. However, the results *in vivo* were dependent on the melanin volume fraction and were inconclusive for 20 % concentration. According to the authors the difference in the results from the two experiments is due to the multiple blood vessels within the PWS and the complex structure of the epidermal-dermal junction. In a previous study, Viator *et al* [38] compared the results for the depth with those from measurements using Optical Doppler Tomography and they were comparable within 20 %. Despite the current difficulties, again the PA technique was the choice for an imaging tool in medicine.

3.5 Monitoring Blood Oxygenation and Brain Functions

Continuous monitoring of the oxygenation of blood is necessary for detecting cerebral ischemia during intensive care of critically ill neurotic patients. Esenaliev *et al* designed an opto-acoustic system to detect laser induced acoustic waves in the superior sagittal sinus, which is a large central cerebral vein. The light of a nanosecond Nd:YAG laser (λ=1064 nm) was delivered via a fiberoptic, a home-made acoustic probe was used to detect the acoustic signal, which was processed with a computer. The results were encouraging and showed that there was a correlation between the parameters of the

opto-acoustic signals and the blood oxygenation.

A similar, but more involved study was conducted by Wang *et al.*[39] They were able to image the blood distribution in rat brain with induced lesions using 532 nm 6.5 ns pulses from Nd:YAG laser. The beam was expanded in such a way that the temperature rise on the skin was less than 20 mK. They not only visualized the brain structure, but also the brain lesions and the cerebral hemodynamics. It was clear that the PA tomography method provides high intrinsic contrast in soft tissues and is completely noninvasive transdermal and transcranial.

Chapter 4

Theory

The Photo-acoustic effect was first discovered by Alexander Bell. [40] He observed that a periodically chopped beam of sunlight incident on a strongly absorbing substance generates audible sound. Since then, the method of photo-acoustics spectroscopy (PAS) has been shown to be effective for many applications, such as non-destructive evaluation of materials, determination of small concentrations and concentration changes in molecular species, [41] heat of formation, photon-induced expansions and contractions of molecules etc. Recently, it has been applied for imaging tumor angiogenesis and measurement of the optical properties of biological tissue.[32, 33, 34, 35] Therefore, PAS is a potential candidate for non-invasive optical biopsy in clinical practices.

The interaction of intensity modulated light with matter can induce several different processes - electrostriction, thermal expansion, photochemistry, molecular dissociation, bubble formation, and breakdown.[42] Temperature and pressure fluctuations are in-

duced in the sample which result in mechanical stress. The efficiency of the PA generation is the smallest for electrostriction and increases towards the breakdown process.

One of the advantages of using this method is that only the absorbed light is converted to sound. Scattered light, which presents such a big problem in conventional medical imaging, does not play a role in the image formation. Consequently, one can obtain images from systems that are optically opaque.

When imaging dental tissue, one needs to consider possible thermal and mechanical damage to the enamel that can lead to non desirable caries attacks. Recently published work on the use of short pulse laser radiation for dental surgery shows that 100 fs pulses crate minimal damage to the surrounding tissue during laser drilling [43].

There are numerous efforts to describe the generation of sound after the absorption of pulsed or continuous light. Before modeling an experiment one need to consider the time and space scales of the experimental setup. For example, in case of weak absorption ($\mu_a l << 1$) the absorbed energy is distributed uniformly along the length of the sample and result in the generation of cylindrical waves, while the strongly absorbing medium ($\mu_a l >> 1$) generates spherical acoustic waves.[44]

The interaction of laser radiation with materials (or tissue) is described using the following quantities. The **stress relaxation time**, $\tau_{sr} = \dfrac{\delta}{v_a}$ is the time needed for the acoustic pulse with speed v_a to travel through the thickness of the irradiated volume.[45] Here δ is the optical penetration depth [mm]. If the **stress confinement condition** is

satisfied

$$\tau_p < \frac{\delta}{v_a}, \tag{4.1}$$

an instant pressure amplitude will be observed prior to the stress wave propagation through the optical zone. During photothermal interactions the energy of the laser beam is converted to heat and then diffused in the medium. The **thermal relaxation (diffusion) time** is the time it takes for the peak temperature rise in a heated region to decrease to 37 % of its total value and is calculated as $\tau_r = \frac{\delta^2}{4\alpha}$, where α is the thermal diffusivity $[cm^2/s]$. Thermal damage is minimized when the laser pulse length τ_p is less than τ_r, also referred as **thermal confinement**:

$$\tau_p < \frac{\delta^2}{4\alpha}. \tag{4.2}$$

The thermal energy distribution is then defined by the laser light distribution. Otherwise, when $\tau_p > \tau_r$ the energy dissipates in the tissue during the pulse.[46, 47] However, it has been observed that in a lot of media, especially biological medium the thermal relaxation takes much longer than the stress relaxation. Thus τ_r can be neglected in most biomedical applications.[45] Photomechanical interactions, such as thermoelastic expansion of tissue or water vaporization can also cause the generation of stress waves in tissue.

The pressure and the temperature changes throughout homogeneous isotropic media are governed by the nonhomogeneous wave equation and the heat transfer equation,

respectively:

$$\nabla^2 p - \frac{1}{v^2}\frac{\partial^2 p}{\partial t^2} = -\frac{\beta}{C_p}\frac{\partial H}{\partial t}, \tag{4.3}$$

$$\kappa\nabla^2 T - \frac{\kappa}{\alpha}\frac{\partial T}{\partial t} = -T_0\beta\frac{\partial H}{\partial t}, \tag{4.4}$$

where H(x,y,z,t) is the density of the electromagnetic energy absorbed and converted into heat per unit volume $[W/cm^3]$, β is the coefficient of thermal expansion $[K^{-1}]$, C_p is the specific heat at constant pressure $[J/kg.K]$, T_0 is the ambient temperature [K], α is the thermal diffusivity $[cm^2/s]$ and v is the speed of sound [cm/s].[48, 49] Since the absorbed energy is directly proportional to the laser energy fluence I, $H \sim \mu I$ we obtain the following relations:

$$\nabla^2 p - \frac{1}{v^2}\frac{\partial^2 p}{\partial t^2} = -\frac{\beta\mu_a}{C_p}\frac{\partial I}{\partial t}, \tag{4.5}$$

$$\kappa\nabla^2 T - \frac{\kappa}{\alpha}\frac{\partial T}{\partial t} = -T_0\beta\mu_a\frac{\partial I}{\partial t}, \tag{4.6}$$

where μ_a is the optical absorption coefficient $[cm^{-1}]$.

Many different solutions for the temperature have been given in the literature depending on the geometry of the environment and the choice of a source. However, they follow a common inverse dependence on the mass density and the specific heat of the material and direct dependence on the absorbed energy. One such solution for spherical geometry and a point source Q is given by McKenzie (1990) [49]:

$$T = \frac{Q}{8\rho C_p(\pi\alpha t)^{3/2}}\exp(-r^2/4\alpha t) \tag{4.7}$$

where r is the distance from the origin. A general solution can be given in terms of the Green functions as follows:

$$T(\mathbf{r},t) = \frac{1}{8\rho C_p(\pi\alpha)^{3/2}} \int_0^1 \frac{dt'}{(t-t')^{3/2}} \int_V q(\mathbf{r}',t') \exp[-(\mathbf{r}-\mathbf{r}')^2/4\alpha(t-t')]dV, \quad (4.8)$$

where $q(\mathbf{r}',t')$ is the heat deposition rate at unit volume. This solution was used by Birngruber to study the heating of pigmented layers of the eye after they were exposed with laser light for 1 s.[50] His source was a Gaussian in space:

$$q(\mathbf{r}',t') = \mu_a I(0) \exp(-2\rho'^2/w^2) \exp(-\mu_a z') \quad (4.9)$$

In this equation I(0) is the incident laser fluence, ρ' is the radial coordinate of the beam, w is the beam radius, and z is the propagation direction.

The generated pressure is directly proportional to the temperature rise in the irradiated volume. If the stress confinement condition is satisfied (Eqn. 4.1) and thermal diffusion neglected, then

$$P = \frac{1}{\gamma}\beta\Delta T = \Gamma\mu_a I(0) \quad (4.10)$$

where $\gamma = (C_P/C_V)(1/\rho C_S^2)$ is the coefficient of isothermal compressibility $[bar^{-1}]$ and $\Gamma = \beta v^2/C_p$ represents the Grüneisen parameter which accounts for the fraction of the heat that generates mechanical stress.[45, 51] The pressure amplitude of the PA wave is proportional to the optical absorption of the medium ($\sim \mu_a I$) while its slope is defined by both, the absorption and scattering (μ_s) coefficients. Thus we define an effective

attenuation coefficient μ_{eff}:

$$\mu_{eff} = (3\mu_a(\mu_a + \mu_s))^{1/2}. \tag{4.11}$$

This means that the acoustic signal contains information about both optical properties of the medium.[34, 45] Its reciprocal value $1/\mu_{eff}$ determines the optical penetration depth in biological tissue. The penetration depth is defined as the distance over which the diffuse energy fluence rate decreases to $1/e$ of its initial value.

Numerous detailed theoretical models of the generated pressure have been suggested. Good historical and theoretical reviews are given by Rosencwaig and Gersho (1976) [52], Sigrist (1986) [48], Vargas [53], Tam (1986) [51] etc. A few solutions of the pressure wave equations will be presented in the following paragraphs.

Both Heretier [54] and Lai [55] independently considered electrostriction in weakly absorbing liquids and showed similar results. The source used by Heritier had a laser intensity Gaussion distribution in both, space and time:

$$I_{her}(r,t) = \frac{2E}{\pi^{3/2} w_0^2 \tau_L} \exp\Big[-\frac{2r^2}{w_0^2} - \frac{t^2}{\tau_L^2}\Big], \tag{4.12}$$

where E is the energy per pulse, w_0 is the beam waist and τ_L is the e^{-1} half width of the laser pulse. The solution for the PA pressure was found to be:

$$p(r_0,t) = \frac{E}{(2\pi\epsilon)^{3/2}} \Big(\frac{v}{r}\Big)^{1/2} \Big(\frac{\mu_a \beta}{C_p} - \frac{\gamma^e}{2ncv^2\epsilon} \frac{d}{dx}\Big) F(x), \tag{4.13}$$

where

$$F(x) = \Big[\Gamma\Big(\frac{3}{4}\Big)_1F_1\Big(-\frac{1}{4};\frac{1}{2}x^2\Big) - 2x\Gamma\Big(\frac{5}{4}\Big)_1F_1\Big(-\frac{1}{4};\frac{3}{2}x^2\Big)\Big]\exp(-x^2). \tag{4.14}$$

$\epsilon = (\tau^2 + w_0^2/2v^2)^{1/2}$ and $x = (t - r/v)/\epsilon$ are the scaled time and space coordinates, respectively, $\gamma^e = \frac{1}{3}(n^2-1)(n^2+2)$ is the electrostrictive coupling constant. ${}_1F_1(\alpha;\beta;z)$ is the degenerate hypergeometric function and $\Gamma(z)$ is the Gamma function.

Lai and Young calculated the pressure using Gaussian, circular and rectangular spacial profiles. Since in the Gaussian distribution is the closest to describing a laser beam profile, we focus on the solution for that kind of a profile:

$$I_{LY} = \frac{E}{(2\pi)^{3/2}C_p w_0^2 \tau_L}\exp\Big[-\frac{r^2}{2w_0^2} - \frac{t^2}{2\tau_l^2}\Big]. \tag{4.15}$$

The solution for the acoustic pressure is given in terms of the Bessel functions $I_{1/4}$ and $K_{1/4}$, and the unit step function Θ as follows:

$$p(r,t) = \frac{E\tau_e^{-3/2}}{8\pi^{1/2}}\Big(\frac{v}{r}\Big)^{1/2}\Big(\frac{\mu_a\beta}{C_p}\frac{d\Phi(t')}{dt'} - \frac{\gamma\tau_e^{-1}}{2ncv^2}\frac{d^2\Phi}{dt'^2}\Big) \tag{4.16}$$

$$\Phi(t') = \sqrt{t'}\exp(-t'^2/4)\Big[\frac{\sqrt{2}}{\pi}K_{1/4}\Big[\frac{t'^2}{4}\Big] + 2\Theta(t')I_{1/4}\Big[\frac{t'^2}{4}\Big]\Big] \tag{4.17}$$

$$t' = (t - r/v)/\tau_e \tag{4.18}$$

$$\tau_e = (\tau_p^2 + \tau_a^2)^{1/2}. \tag{4.19}$$

These two results are essentially equivalent. Their differences are due to the slightly

different shapes of the laser beam profiles and methods of solution.

The formalism for the pressure in solids is not much different, except that electrostriction is ignored. In case of ablation of metals with ultra-short laser pulses one has to consider the non-equilibrium heating of the electrons and the lattice. To evaluate the temperature, the two-step parabolic model needs to be applied. The model is described by two coupled differential equations for the electron and lattice temperatures.[56] As a dielectric, porcelain is a poor thermal and electric conductor. However, high irradiance laser radiation ($\sim 10^{14} W/cm^2$) can ionize dielectrics and produce electrons that may dominate the absorption in a similar manner as the free carriers in metals.[57] The results presented in this paper were obtained using much smaller irradiance and such a formulism is unnecessary. On the other hand, ablation is something we want to avoid in dental diagnostics and will not be considered in this study.

The propagation of the generated sound wave depends on the elastic properties of the medium. The velocity of the wave

$$v = \sqrt{\frac{E}{\rho}} \tag{4.20}$$

is proportional to the Young's modulus E, which is defined as the ratio of stress vs. strain in the material. It also determines the natural frequency of the material:

$$w = A\sqrt{\frac{E}{\rho L^2}}. \tag{4.21}$$

Here A is a coefficient that depends on the way the sample is attached to its base.

As they spread through the medium, sound waves will be scattered, reflected and absorbed. When the wave encounters a boundary between two media with different impedances it can be transmitted into the second medium. Reflections from boundaries that are much larger than the wavelength of the wave are called specular (or mirror-like). If the wavelength is comparable with the dimensions of the obstacle or the surface irregularities, the incident wave will be scattered (diffused). The time it takes for the wave to return to the transducer determines the distance to the obstacle. This process is widely used in medical ultrasonic devices. In fact, ultrasonic imaging of teeth has been demonstrated be able to successfully define the dentinoenamel junction and the pulp wall in teeth.[15, 16]

Chapter 5

Computations and Results

5.1 Introduction

The advantages of using femto-second laser radiation for precise material processing have been demonstrated by several authors.[43, 58] In the applications of laser drilling and laser ablation femtosecond laser radiation creates minimal thermal and mechanical damage to the surrounding area.[43, 59] Therefore, it is reasonable to use femtosecond laser pulses for the development of a tool for dental practices. The temperature profile can be controlled temporally and spatially which is beneficiary for photo-acoustic imaging. The pressure amplitude during drilling of a dentine slice with femto-second pulses is 2 to 3 orders of magnitude lower than the acoustic transients created by nanosecond pulses.[43] This is important, because generation of microcracks of several tens of microns to the enamel would result in new carious attacks and thus defeat the treatment process. The non-destructive pressure wave generated when the optical absorption in-

duces a resonance will overcome the limitations of conventional ultrasonic imaging inside teeth. Furthermore, there are currently no diagnostic tools available that may image soft tissue health inside teeth. Photo-acoustic imaging aims to overcome these obstacles. In the presented work on the photo-acoustic effect, the temperature effects of pulsed laser - tissue interaction will be discussed first.

The focus of this chapter is the calculation of the temperature rise in dental porcelain due to the interaction of the laser radiation with dental porcelain material.

5.2 Computational Model

The absorbed laser light will heat up a local volume and generate a sound wave. As a result of the Boyle-Gay Lussac law, an increase in the temperature will result in an increase in the local pressure. The conversion efficiency of optical energy to acoustical energy depends on the temperature gradient generated inside the sample. For laser pulse duration shorter than the material thermalization time of approximately 1ps, electrons and the lattice are not in thermal equilibrium.[60] Due to differences in the specific heat capacities, electrons reach a different temperature distribution than the lattice. The process is nonlinear, because the specific heat of the electrons depends on the temperature.[61] Normally, this process is described by the hyperbolic two-step model, which consists of a pair of coupled partial differential equations.[56] This model can be used later to describe the heating of metal dental crowns. The focus of the work presented here is the calculation of the temperature distribution inside a slab of dental

porcelain. As a dielectric, porcelain is a weak thermal and electrical conductor. However, high intensity laser pulses ($\sim 10^{14}\ W/cm^2$) can ionize dielectrics and generate free electrons that would dominate the absorption in a similar manner as the free carriers in metals.[57] Since any ablation of the tooth surface is highly undesirable for imaging purposes, we consider here intensities that are well below the ionization threshold. For intensities in the order of $10^6\ W/cm^2$ one can describe the temperature distribution by the heat transfer equation below, including the initial condition and assuming homogeneous boundary conditions:

$$\nabla^2 T(\vec{r},t) - a^2 \frac{\partial T(\vec{r},t)}{\partial t} = -\frac{S(\vec{r},t)}{\kappa} \tag{5.1}$$

$$T(\vec{r},0) = T_0(\vec{r}), \tag{5.2}$$

where $a^2 = \rho c/\kappa$, ρ is the mass density of the material $[kg/cm^3]$, c is the specific heat capacity [J/kg.K], κ is the thermal conductivity [W/kg.K], and T is the temperature [K]. The source term $f(\vec{r},t) = -S/\kappa$ describes the absorption of the laser energy, where $S \sim \mu_a J$. Here μ_a is the optical absorption coefficient $[cm^{-1}]$, J is the laser flux $[J/cm^2]$, and z is the depth of penetration. The solution of eqn. 5.1 for the temperature is given in terms of the Green's function as follows:[62]

$$\begin{aligned} T(\vec{r},t) = & \int_0^t \int_V G(\vec{r},t;\vec{r}',t') f(\vec{r}',t') d\tau dV(\vec{r}') \\ & - a^2 \int_V G(\vec{r},t;\vec{r}',0) T_0(\vec{r}') dV(\vec{r}'). \end{aligned} \tag{5.3}$$

Here, the heat source $f(\xi, \tau)$ is modeled as a Gaussian distribution in space. Since femtosecond pulses are much shorter than the time to reach thermal equilibrium (approx 1ps), it is reasonable to approximate the time component of the source function with a Dirac delta distribution.[60, 63]

$$f(\vec{r}', t') = -\frac{(1-R)}{\kappa}\mu_a J \exp[-\mu_a z] \exp\Big[-\frac{2(\vec{r}')^2}{\omega^2}\Big]\delta(t), \tag{5.4}$$

$$\omega(z) = \omega_0\Big(1 + \Big(\frac{\lambda(z-z_0)}{\pi\omega_0^2}\Big)^2\Big)^{1/2}, \tag{5.5}$$

where R represents the surface reflectivity, z_0 is the location of the minimum waist ω_0, λ is the wavelength, and ω is the beam radius [cm]. The Green's function can be written as:

$$G(\vec{r}, t; \vec{r}', t') = -\Big[\frac{a^2}{4\pi(t-t')}\Big]^{\frac{3}{2}} \frac{1}{a^2} \exp\Big[-\frac{a^2}{4}\frac{|\vec{r}-\vec{r}'|^2}{t-t'}\Big]. \tag{5.6}$$

For spherical polar coordinates, the solution for the temperature becomes:

$$T = T_0 + \frac{2(1-R)\alpha J}{\rho c(1+\tau)^{3/2}} \exp[-\alpha z] \exp\Big[-\frac{r^2}{w^2(1+\tau)}\Big], \tag{5.7}$$

where $\tau = 8t/a^2\omega^2$ is the scaled time. The maximum of the temperature rise is directly calculated from Equ. 5.7 and for $r \geq \omega$ occurs at the time

$$t_{max} = \frac{a^2\omega^2}{8}\Big(\frac{4}{3}\frac{r^2}{\omega^2} - 1\Big). \tag{5.8}$$

Table 5.1: Thermophysical properties of dental tissue

Tissue	Enamel	Dentin	Pulp
Thickness [mm]	1.5	1.0	5.0
Density [g/cm^3]	3.0	2.0	1.027
Thermal conductivity [mJ/g.K]	9.2	6.3	5.72
Specific heat [J/g.K]	1.1	1.17	3.93
Optical absorption at 750 nm [cm^{-1}]	1.0	6.0	4.5

At the spatial location $r = \omega_0$, the maximum temperature rise occurs at $\tau_{max} = 0.33$, when inserting the value for a^2, for the focal waist $\omega_0 = 35\ \mu m$, one finds $t_{max} \approx 300\ \mu s$. For tighter focusing to $\omega_0 = 1\ \mu m$, the temperature maximum occurs at $t_{max} \approx 0.3\ \mu s$. Table 5.1 shows typical values for the thermophysical properties of dental tissue. A minimal temperature rise induced by the laser radiation is desirable for application in dental imaging. Tighter focusing will allow us to increase the spatial resolution of the imaging, yet higher peak irradiances and temperature maxima will result. The pressure generated as a result of the heating is directly proportional to the temperature rise:[33]

$$\Delta P = \frac{1}{\gamma}\beta\Delta T, \tag{5.9}$$

where β is the volume expansion coefficient $[K^{-1}]$, $\gamma = c_p/c_v\rho c_s^2$ is the coefficient of isothermal compressibility $[P/a]$, c_v and c_p are the heat capacities at constant volume and pressure in units of $[J/g.K]$, respectively, and c_s is the sound velocity in the medium.

5.3 Numerical Results

The solutions of the equation for the computational model are found by applying Gear's method that is normally used for solving stiff systems od differential equations. Gear's method is appropriate, because the femto-second laser pulses require different time scales for the laser excitation and the thermal diffusion. This numerical approach is stable for variable time steps, which means that the errors will diminish instead of grow with time. Gear's method has been implemented in the IMSL routine MOLCH, which allows one to solve systems of partial differential equations. For our purposes the routine was adapted to solve the heat transfer equation only. The Gear method is predictor-corrector algorithm that uses only three previous steps unlike the four previous steps required by the Adams-Moulton and Milne's method.[64] The FORTRAN source code is given in the Appendix.

A 0.9 ms laser pulse with 900 mJ energy will rise the temperature on the surface of a dentin layer with 217 degrees, while a 90 ms pulse with the same energy will rise the temperature with 150 K. The laser beam has a radius of 0.4 mm and a wavelength 1064 nm. Figures 5.1 and 5.2 illustrate the computed temperature rise after the interaction with the nanosecond laser radiation. The results are compared with numerical data published by Moriyama *et al* [65].

Moriyama's data was generated by solving the heat transfer equation using the Crank-Nicolson's finite difference method. It can be seen that the data differs, but the maximum temperature rise coincides in the case of 0.9 ms pulses. The differences could

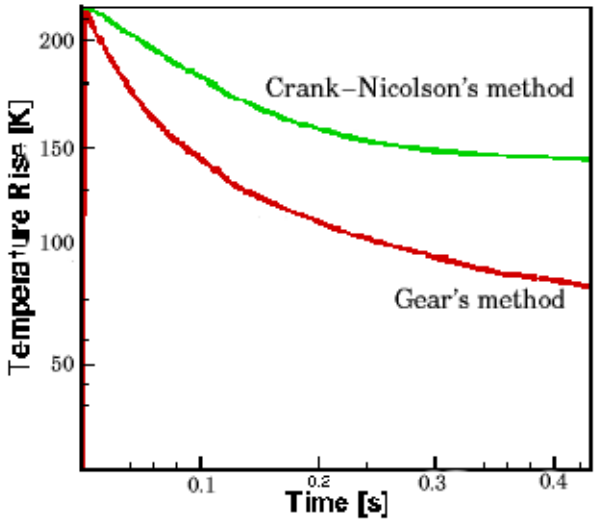

Figure 5.1: Temperature rise on the surface of a dentin layer after interaction with 0.9 ms laser pulses. Red line - Gear's method and Green line - Crank-Nicolson's method

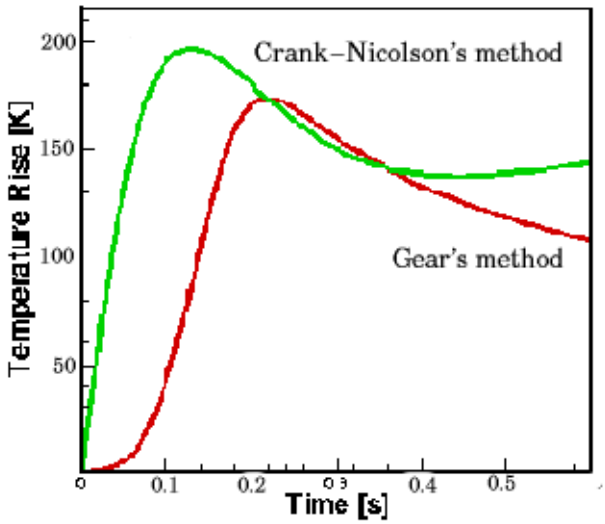

Figure 5.2: Temperature rise after the interaction of the porcelain cube with the Nd:YAG laser radiation. Red line - Gear's method and Green line - Crank-Nicolson's method

be explained with the fact that the assumptions for the source are considerably different in Moriyama's paper. It involves the Beer-Lambert law for the intensity attenuation with depth and the temporal dependence is not given explicitly.

This is a reasonable approach because the 90 ms pulses, for example, are longer than the thermal diffusion time and the thermal confinement condition (Eqn. 4.2) is no longer satisfied. This means that the thermal energy propagates into the tissue during the laser pulse. both the thermal and the stress confinement conditions (see Eqn. 4.1) are applicable for femto-second pulses. The main purpose of this calculation was to investigate the order of magnitude of the temperature rise in order to proceed with simulating the experimental data[1].

Since picking a single femto-second pulse was not possible at the time, trains of pulses were generated using a mechanical shutter. Numerically this was modeled as a long 40 ms and 8 ms pulse. The results on Fig. 5.3 and Fig.5.4 show that a beam with a fluence of 3 J/cm^2 heats the surface of the porcelain crown with 7.5 $^{\circ}C$ and 1.5 $^{\circ}C$ at the center of the beam. As expected, the curve at the edge of the beam has a maximum later in time showing the heat diffusion process across the irradiated area. Comparison with the experimental data, given in Fig. 6.15 and Fig. 6.16 would show a reasonably good agreement between them. These differences originate from errors due to the irregular opening of the mechanical shutter, from insufficient time for the material to cool down between openings and/or noise from the thermocouple. Figure 5.5 shows

[1]Experimental set up and results are given in detail in Chapter 6

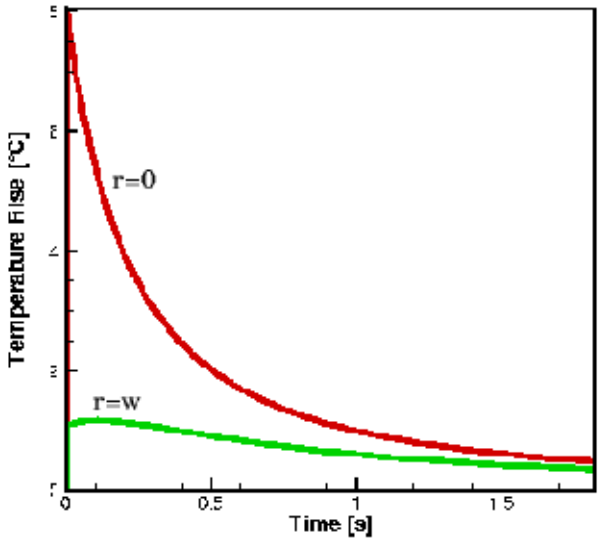

Figure 5.3: Temperature rise on the surface of a dental crown after interaction with 40 ms train of 70 fs laser pulses.

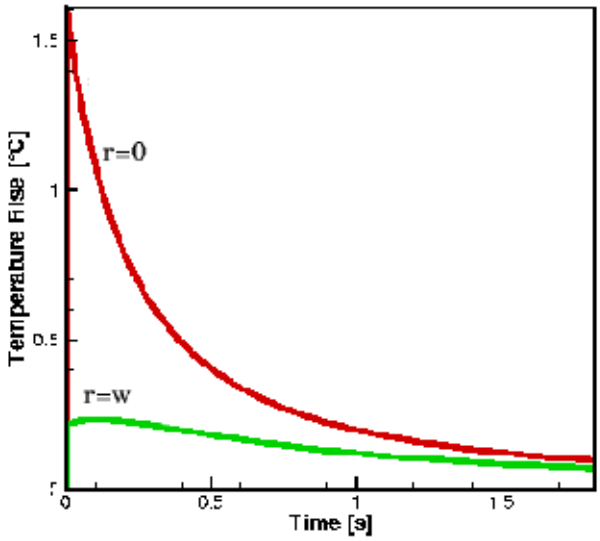

Figure 5.4: Temperature rise on the surface of a dental crown after interaction with 8 ms train of 70 fs laser pulses.

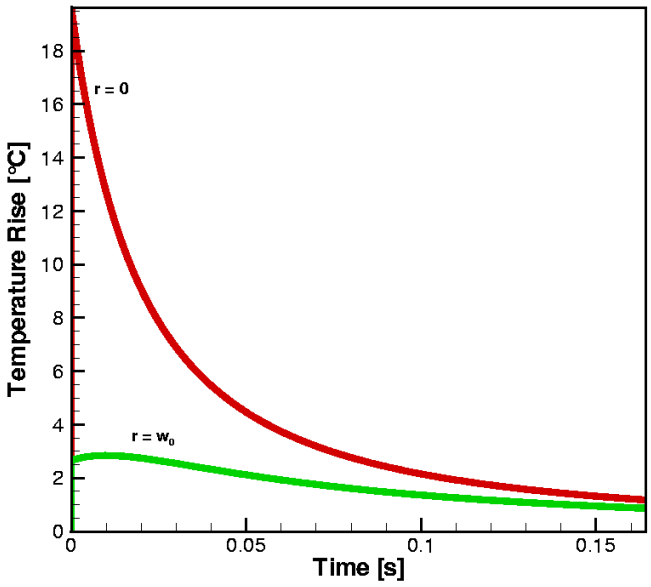

Figure 5.5: Temperature rise on the surface of a dental porcelain cube after interaction with 8 ns laser pulses.

the calculation of temperature rise from the heating of the cube with nano-second laser pulses with fluence of about 2 J/cm^2.

Chapter 6

Experiments and Results

This chapter has been divided into two major parts showing the results of the experiments performed with Nd:YAG and Ti:Sapphire laser radiation, respectively. Presented are measurements of the acoustic signal in the presence or absence of liquid in the material as well as the temperature rise from both ceramic phantom and a dental crown.

6.1 Studies with Nanosecond Laser Radiation

6.1.1 Detecting the Presence of a Liquid Under the Surface of Porcelain Material

A Q-switched Nd:YAG laser (Quantel International), operating at the fundamental wavelength of 1064 nm was used as a radiation source in the experiments. The laser pulse width was 8 ns, and the repetition rate was 10 Hz. The laser beam was focused on the sample surface to a spot size of 0.3 mm which resulted in an irradiated area of

0.28 mm^2. A polarizer-analyzer pair was used to vary the energy per pulse in order to evaluate the ablation threshold for the material. A polymer ultrasonic transducer detected the sound waves generated in the sample. The transducer was a 28 μm thick Polyvinylidene difluoride (PVDF) film with active area of $7 \times 7\ mm^2$ and a bandwidth of about 100 MHz. The sample was a 7.63 mm cube made of dental porcelain (Excelco®). A canal with a diameter of 1.38 mm was drilled in the middle of the cube to simulate a blood vessel. The detector was directly attached to the sample and the acoustic signals were monitored and recorded by a Tectronix TDS 3054 oscilloscope.

The purpose of the initial measurements was to evaluate the possibility of recording an acoustic signature indicating the presence of liquid under the surface of the porcelain phantom. For these experimental investigations optical breakdown was created in the air, close to the surface of the sample. Figure 6.1 shows the Fourier transform of the signal when no liquid was present. Multiple reflections are distinguishable around the 2 MHz peak indicating the natural frequency of the porcelain material. The resonance frequency of the sample material was estimated by the use of Eqn. 4.21. Subsequently, the canal was filled with 30 per cent intralipid (IL) solution. Figure 6.2 shows the results. The Fourier transform of the data in Fig. 6.2 consists of a frequency spectrum that is slightly shifted and attenuated compared to the hollow canal result. Comparisons of the results indicate that the suggested method is viable and needs further investigation.

Additional measurements were performed using lower energy per pulse. The laser beam was focused into the canal to a waist of 0.3 mm and the energy per pulse was 5.3

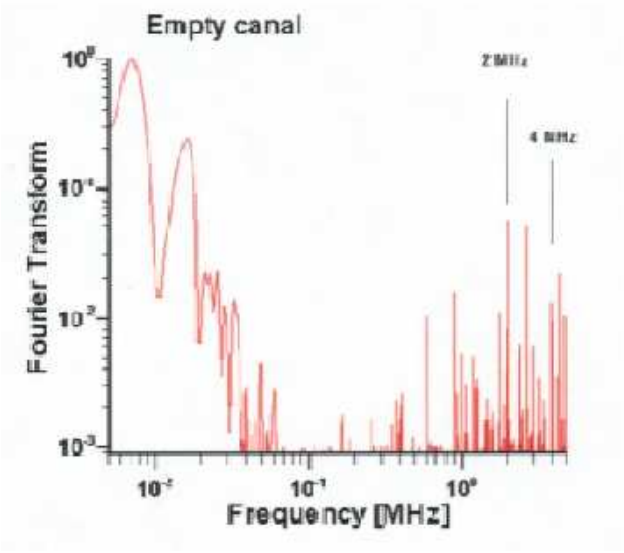

Figure 6.1: Fourier transform of the signal from the porcelain cube with empty canal

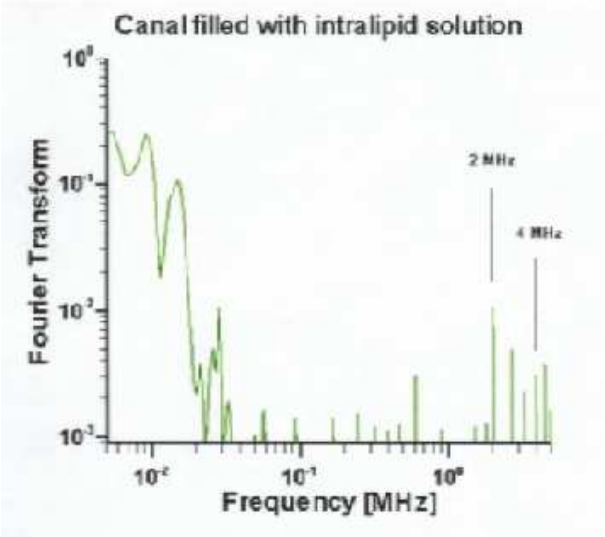

Figure 6.2: Fourier transform of the signal from the porcelain cube with 30 per cent IL solution in the canal

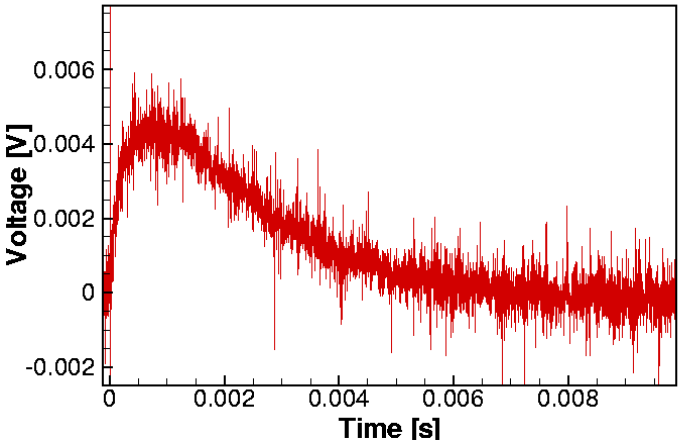

Figure 6.3: A typical signal from the PVDF transducer after 8 ns laser pulse.

mJ. The recorded temperature increase on the surface was 10°C. A raw result for the acoustic measurement is illustrated in Fig. 6.3. Figures 6.4 and 6.5 show the Fourier transforms of the data for empty and full canal. These results indicate that the presence of liquid can be detected using much lower energies.

Ablation is not desirable during imaging of teeth; however, it is of interest to investigate the ablation threshold for the porcelain material. For this purpose, the energy of the laser beam was gradually increased until there was a noticeable difference in the acoustic spectra. The laser beam was focused on the surface of the porcelain material and the energy per pulse was 20 mJ. Fig. 6.6 shows the recorded data. Fig. 6.7 shows that increasing the energy to 40 mJ caused additional reflections to appear at the beginning of the signal.

It is interesting to note that acoustic monitoring of ablation of tissue has been considered for treatment of burned skin.[66] The reported data in the literature suggests

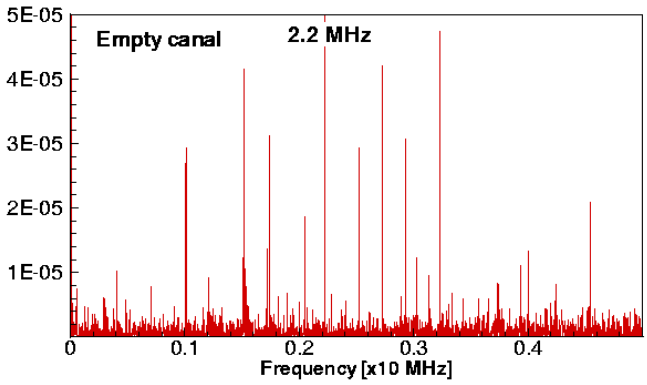

Figure 6.4: Fourier transform of the signal from the porcelain cube with no IL solution in the canal

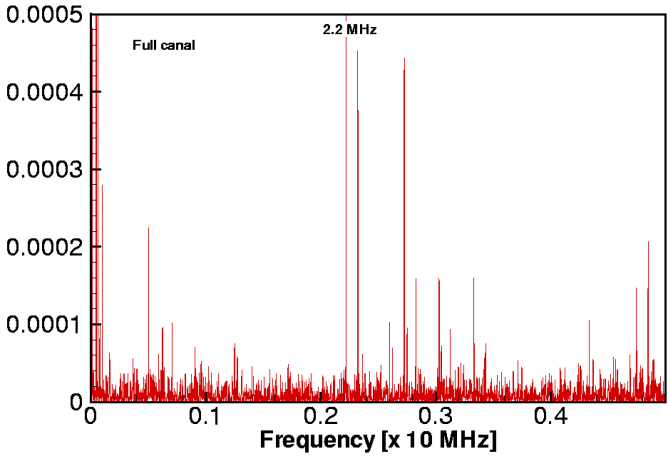

Figure 6.5: Fourier transform of the signal from the porcelain cube with 30 per cent IL solution in the canal

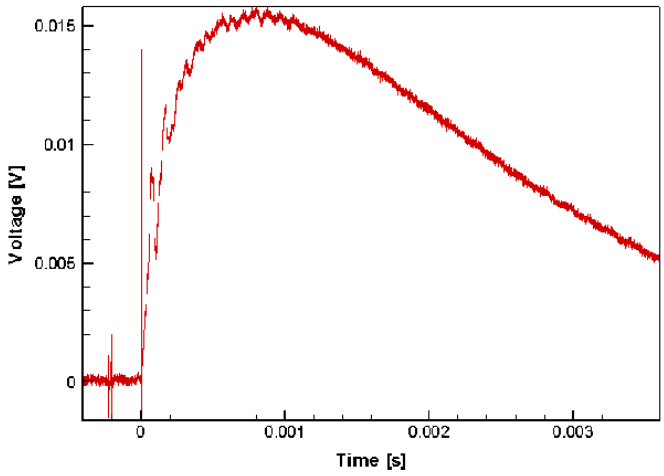

Figure 6.6: Acoustic signal generated with 20 mJ energy per pulse.

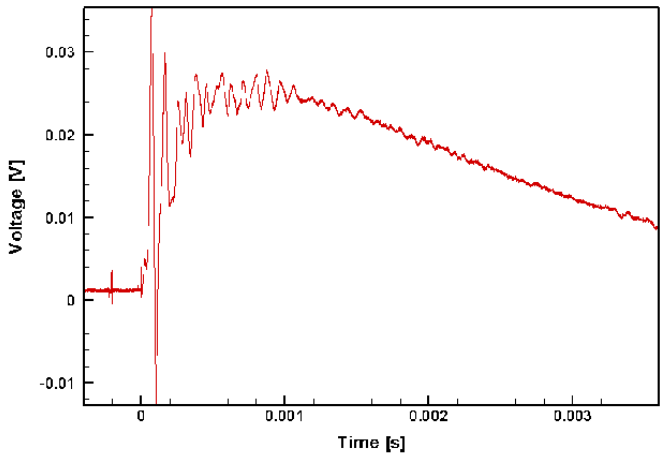

Figure 6.7: Ablation spectrum generated with 40 mJ energy per pulse.

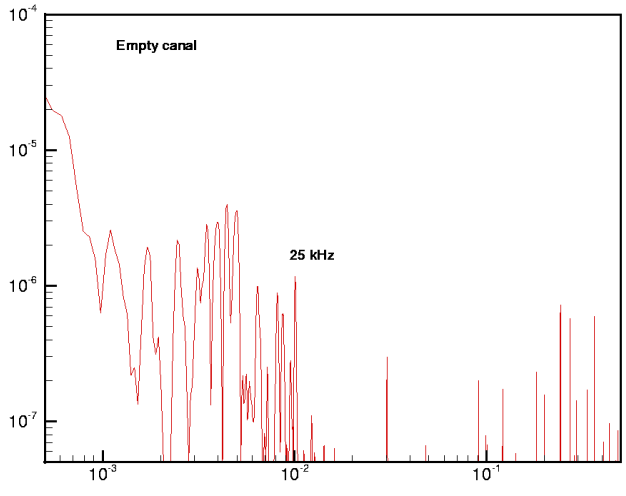

Figure 6.8: Fourier transform of the signal from the porcelain cube with no IL solution in the canal after ablation.

that the acoustic spectra could clearly distinguish healthy from necrotic tissue. Such differences occurred as well in the experiments performed during the course of this work. Figure 6.8 shows the Fourier transformed data from the empty canal. Figure 6.9 shows the Fourier transformed results from the filled canal. The comparison of the recorded sets reveals that considerably more reflections occur in the empty canal.

6.1.2 Measuring the Temperature Rise on the Surface of the Porcelain Material

From a medical point of view, it is important to understand the interaction of tissue with short pulse laser radiation. The temperature rise in the area of interest can determine the effects, including the possible side effects, from the visualization and/or the

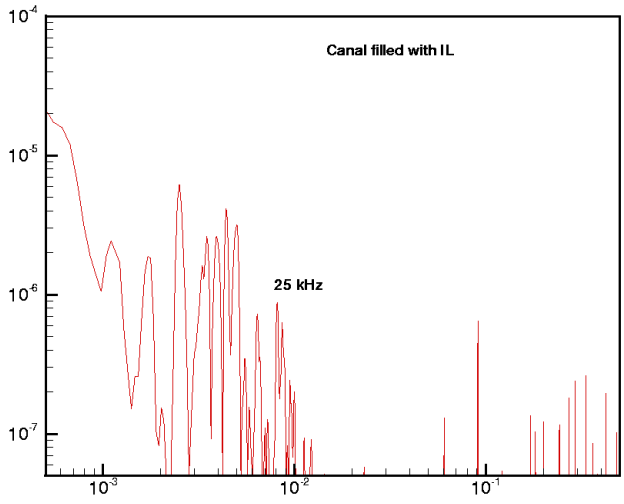

Figure 6.9: Fourier transform of the signal from the porcelain cube with 30 per cent IL solution in the canal after ablation.

treatment. The magnitude of the generated pressure as a result of the laser heating can indicate the possibility of damage. In a preliminary study, the temperature rise was measured on the surface of the porcelain cube (Excelco®), following a nanosecond laser irradiation. The laser radiation was generated in a Q-switched Nd:YAG laser cavity (Quantel International). Figure 6.10 illustrats the experimental setup. The energy of the 8 nanosecond laser pulses was 16.8 mJ at the wavelength of 1.064 μm. The light was focused using a focusing lens (not shown) to the surface of the porcelain cube. The temperature rise was detected with a fast response, small diameter (76 μm) thermocouple (Omega®, Chromega®-Constantan type E) and the data was acquired using a National Instrument A/D converter with customized software. For this measurement, the beam diameter on the surface of the tooth was 3 mm, with incident flux of about 26

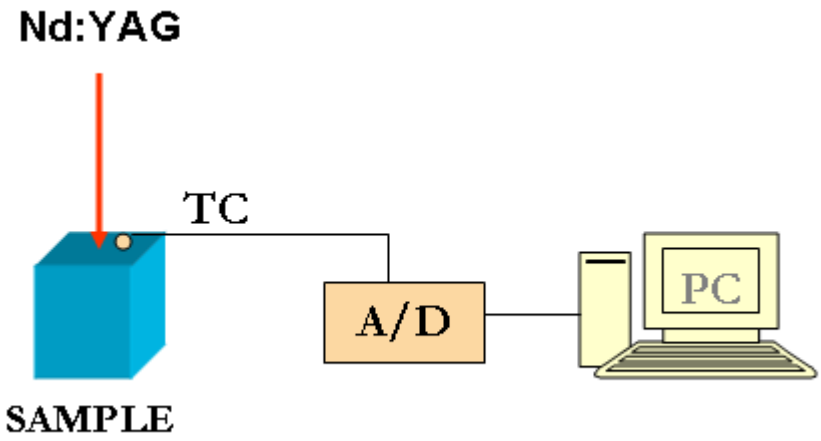

Figure 6.10: Schematic of the experimental setup to measure the temperature rise on a porcelain cube with the Nd:YAG laser

MW/cm^2 and a fluence of 215 mJ/cm^2. Figure 6.11 shows that the result of a maximum temperature rise of about 25°C. The presence of the thermocouple on the beam spot has been assumed to have a negligible effect because of the small size of the tip. The 10 Hz noise that appears in the data is due to the flash lamp charging of the laser. It has been reduced numerically by the use of a digital, Savitzky-Golay filter.[67]

6.1.3 Measuring the Temperature Rise on the Front and Back Surface of a Dental Crown

The same setup was used for these measurements as shown in Fig.6.10. The measured energy per pulse was 15 mJ and the beam diameter on the surface was 3 mm. The dental crown (Procera®) was positioned in such a way that the top surface was perpendicular to the laser beam. The thermocouple was positioned off the center of the beam. The results from the measurements show a slightly lower temperature rise, partially due to

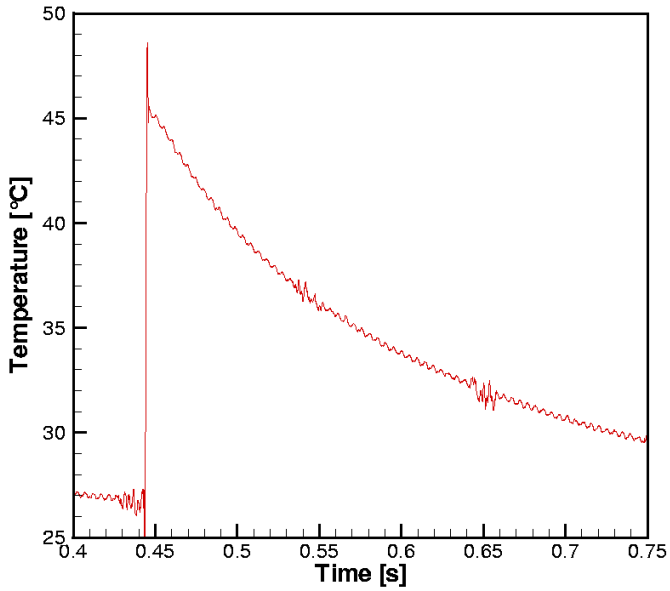

Figure 6.11: Temperature rise after the interaction of the porcelain cube with the Nd:YAG laser radiation

the lower energy of the pulses. Figures 6.12 and Fig. 6.13 show the Fourier transform of the data. The temperature rise on the surface of the crown was about 10 degrees. The temperature on the back side was taken at the same location as on the surface and the resultant temperature rise was measured to be about 2 degrees. The thickness of the crown is measured to be about 2 mm.

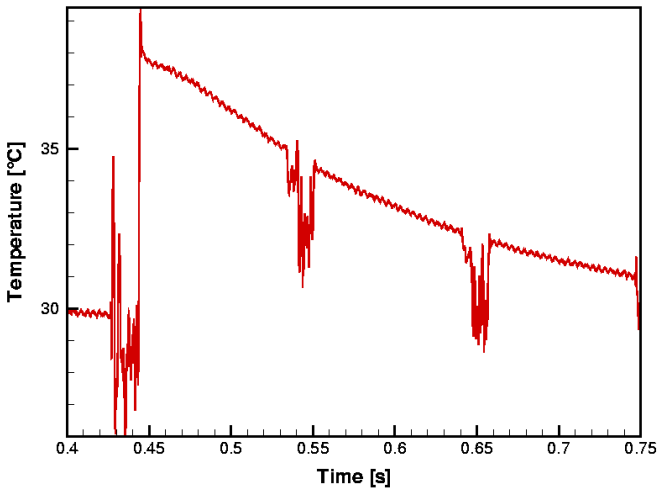

Figure 6.12: Temperature rise on the surface of a dental crown after the interaction with the Nd:YAG laser radiation

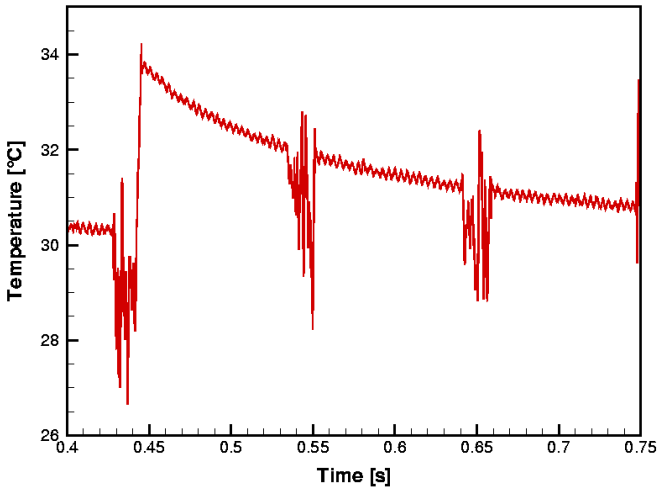

Figure 6.13: Temperature rise on the back surface of a dental crown after the interaction with the Nd:YAG laser radiation

6.2 Studies with Femto-Second Laser Radiation

6.2.1 Measuring the Temperature Rise on the Front and the Back Surface of a Dental Crown

For the experimental studies 70 fs near-infrared radiation from the Spectra Physics model Tsunami Ti:Sapphire laser was used with 7.3 nJ energy per pulse . The wavelength and the laser beam radius were, respectively, 820 nm and 1 mm. In this investigation 8 ms and 40 ms pulse trains of 70 fs laser pulses were used. These pulse trains were obtained with a mechanical shutter. Single 70 fs pulse measurements will be of interest in future experimental work. The use of pulse trains allows one to employ the unfocused beam diameter of 2 mm to keep the irradiance of individual pulses at approximately $3 \times 10^6 W/cm^2$, and to increase the temperature well into the thermocouple's range. For comparison, the fluence of about 0.76 J/cm^2 that is deposited during the 40 ms is comparable with the measured threshold of 0.6 J/cm^2 for single-pulse ablation of enamel.[43] The temperature is measured with a fast response thermocouple (Omega®, Chromega®-Constantan type E, 0.003') whose readings are recorded with a National Instruments analog to digital converter and a customized software (see Fig. 6.14). The experimental data shows that the temperature on the surface of the crown raised by 2.5°C after a 8 ms exposure (Fig. 6.15) and about 5°C after a 40 ms exposure (Fig. 6.16). Measurements on the back of the crown did not lead to any noticeable change, but 800 ms exposure showed a steady increase of about a degree as shown in Fig. 6.17.

Data on the temperature rise given in the literature relates to different types of tissue

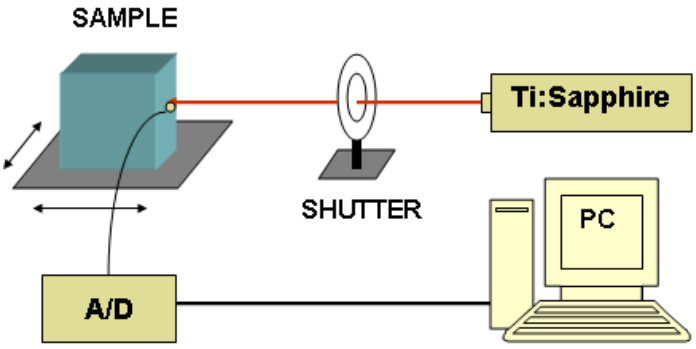

Figure 6.14: Schematic of the experimental setup to measure the temperature rise on a porcelain crown with the Ti:Sapphire laser

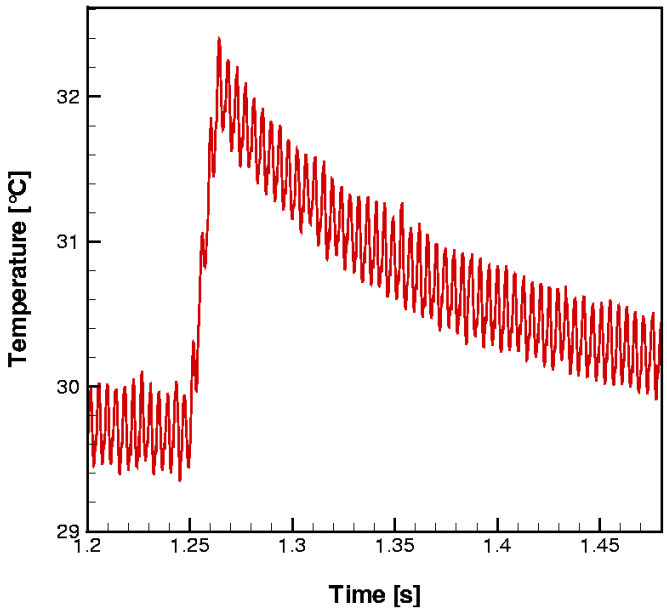

Figure 6.15: Temperature rise on the front surface of a porcelain crown with an 8 ms exposure with femto-second laser pulses

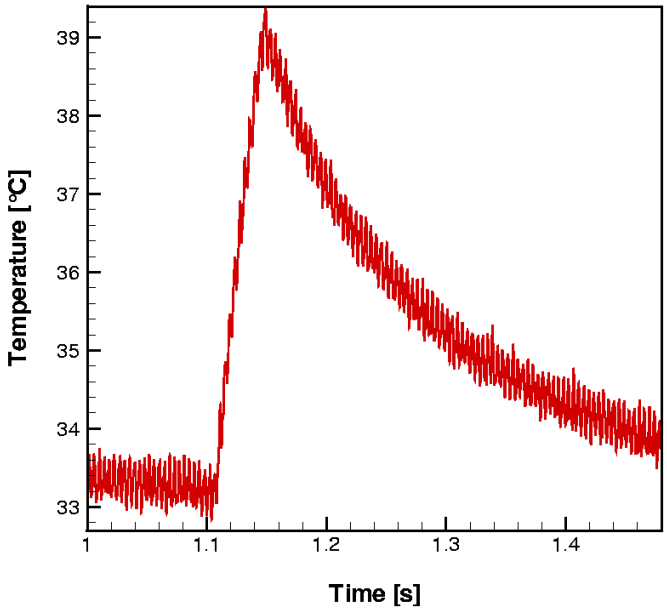

Figure 6.16: Temperature rise on the front surface of a porcelain crown with an 40 ms exposure with femto-second laser pulses

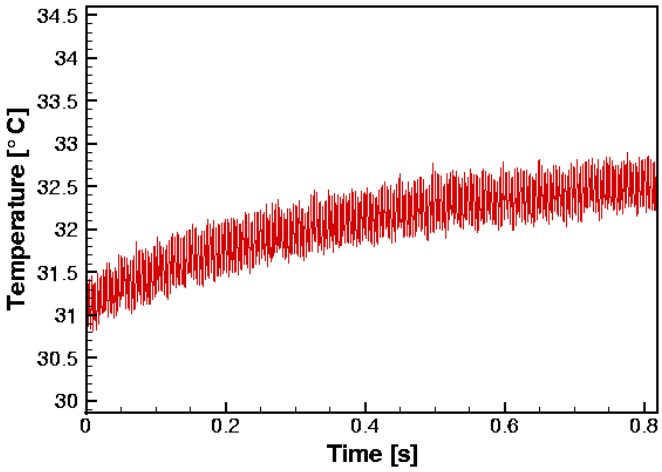

Figure 6.17: Temperature rise on the back surface of a porcelain crown with a continuous exposure with femto-second laser pulses

- dentin, soft tissue,and retina.[47, 63, 65, 68, 69] The published literature suggests that on average a fluence of 1 J/cm^2 will cause an increase of 1-2 °C in 10-20 ms exposure time. The total fluence per 8 ms irradiation time is approximately 1 J/cm^2; therefore, the measured value of 2.5 °C agrees well with values found in the literature. During the 40 ms exposure, the 3 J/cm^2 delivered to the material increased the temperature by 5 °C. The measured temperature increase also agrees with the above presented numerical and analytical results.

6.2.2 Temperature and Pressure Measurements Using Dental Porcelain Material

For the purpose of generating a stronger pressure amplitude by increasing the temperature on the surface of the porcelain cube (see Eqn. 4.10), the laser beam was focused using a lens with a focal length of 125 mm. The focal beam diameter is $d \sim 2f^{\#}\lambda$, where $f^{\#} = f/D$ is the f-number, defined by the focal length f of the lens and the diameter of the beam D.[70] Furthermore, the depth of focus, or the Rayleigh range is given by $2z_R = 6.28(f^{\#})^2\lambda$. Therefore, the beam diameter of 2 mm was reduced to $100\mu m$ and the Rayleigh range of 20 mm was enough to cover the thickness of the porcelain material. The energy per pulse of 7.3 nJ delivered in 7 ms trains of pulses defined a fluence of 13 J/cm^2. Figure 6.18 shows that the increase in temperature varied from 8 to 13°C. This variation of the temperature is due to the variable opening time of the shutter. Figure 6.19 shows a 7 ms exposure caused an increase of 8 °C.

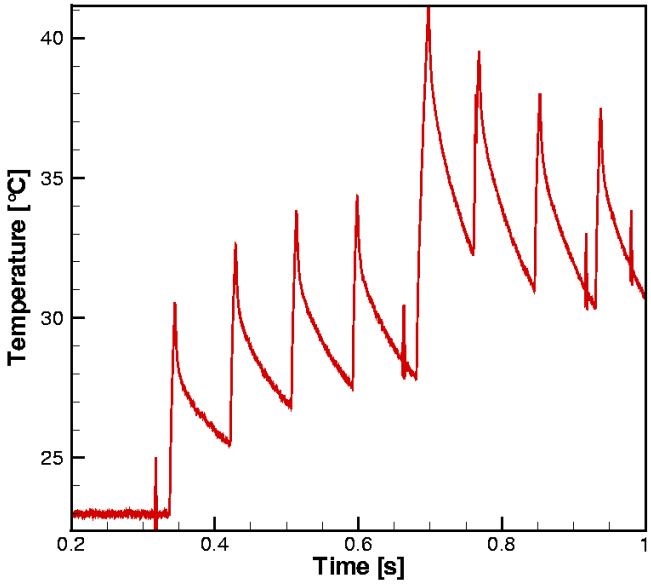

Figure 6.18: Temperature rise on the surface of a porcelain cube using a mechanical gate

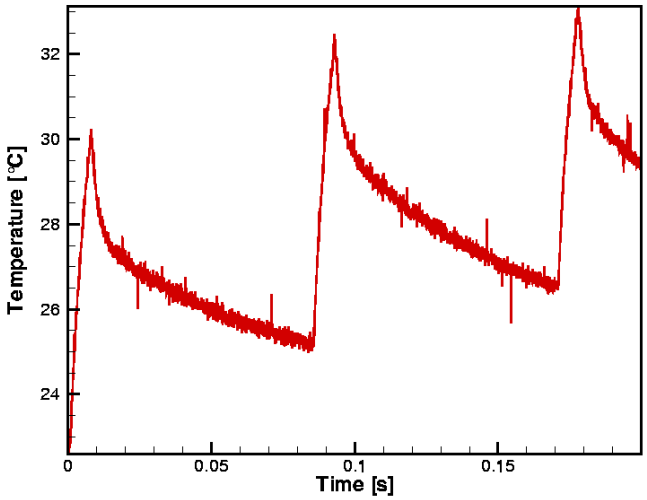

Figure 6.19: Temperature rise on the surface of a porcelain cube using a mechanical gate - 8ms exposure

Chapter 7

Discussion and Future Work

A measure of the vitality of dental pulp is valuable for maintenance of the health of the teeth. The proposed method for photo-acoustic detection of blood underneath natural and artificial dental crowns can be realized in a portable diagnostic instrument. Figure 7.1 [71] illustrates how this instrument is envisioned. A fiber optics device will deliver the laser pulses. The wavelength will be chosen such that it has large differences in the absorption coefficients of blood and the ceramic material. The absorption of the light will create a pressure wave that will be detected with a multi-sensor array. What has been investigated in this work, computationally and experimentally, is the temperature rise on the surface of the dental material and the generated pressure amplitude. It will be beneficial to include non-linear interaction in future work, to obtain additional information for the state of teeth and the properties of the material. Image acquisition and image reconstruction solution is of interest to generate a 3-D image of the blood

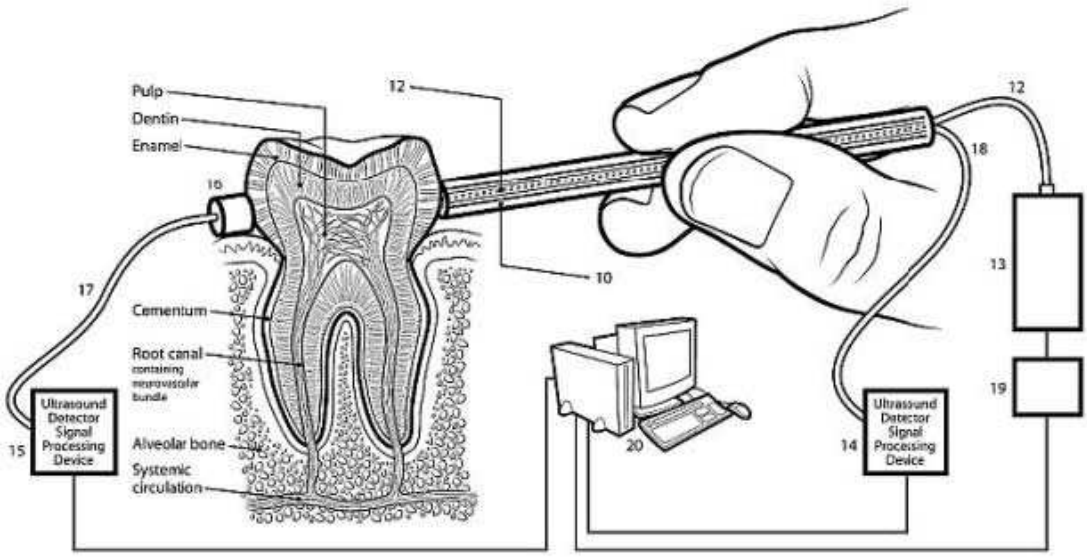

Figure 7.1: Schematic for photo-acoustic imaging

supply in the tooth.

7.1 Data Acquisition

It is envisioned to deliver the light to the tooth using a fiber optic cable. Fiber optic cables are widely used for medical applications because of their flexibility and a small diameter, which allows better access to different tissues in the body with minimal discomfort for the patient. Light is delivered directly to the target without requiring the end user to perform a sophisticated optical alignment procedure.

As it is mentioned earlier in this work, the choice of femto-second laser radiation is based on their confined interaction with the material without unnecessary damage to the surrounding medium. The interaction is thermally confined and the heat diffusion

is limited by the laser light distribution. Femto-second lasers are predominantly used in research today. Also, these short pulsed lasers are becoming increasingly popular for medical and industrial applications. This is also due to their size, pump laser requirements, price and need for regular realignment. However, recent developments have overcome some drawbacks by introducing direct pumping from fiber coupled laser diodes and light propagation inside waveguides. Consequently, companies have just introduced a compact fiber based femto-second source, which is portable, stable and offers a fiber coupled output. Therefore, the size of the source and its stability is no longer an issue for dental imaging.

The axial resolution is defined as the minimum reflector separation required along the direction of the beam to produce separate echoes. It is equal to half the coherence length or half the spatial pulse length for optical and ultrasonic sources, respectively. The coherence length of a Ti:Sapphire laser with a wavelength of 840 nm and a spectral bandwidth of 10 nm can be estimated using the following relation:

$$l_c = \frac{2ln2}{\pi}\left(\frac{\lambda^2}{\Delta\lambda}\right) \approx 31\mu m. \tag{7.1}$$

This means that the axial resolution is typically 15 μm. It was reported in the literature that the length of the laser pulses is important as well. For example, Oraevski et al. reported that 15 ns laser pulses limited the resolution to 25 μm [33]. Sub- 10 fs pulses have been shown to reduce the resolution down to 0.75 μm.[72]

One of the concerns with measuring the temperature on the surface of the phan-

tom with the Ti:Sapphire laser was the inability of the available mechanical shutter to maintain constant opening times and a large minimum opening time. This problem can be solved by using a pulse picker. Pulse pickers are used to selectively pick pulses from the pulse train of a femto-second laser. One can also use a Pockel cell as an ultrafast shutter. A Pockel cell contains a crystal that becomes birefringent when high voltage is applied. If two polarizers are placed on both sides of it, polarized light incident on the modulator cannot pass through the analyzer unless voltage is applied. The speed of these devices, i.e., the rate at which they can be turned on and off, can reach 8 GHz. They are faster than the acousto-optical shutters, but have higher voltage requirements.

The ultrasonic detection is an important component of the acquisition system is the ultrasonic detector. In the experiments a piezoelectric polymer sensor (PVDF film) was used. The PVDF film is attractive for medical applications because of the following properties: (i) wide bandwidth of 1-100 MHz; sensitivity in the order of 30 $\mu V/Pa$ [32]; (ii) acoustic impedance that matches water, human tissue and "over-the-counter" adhesives, and (iii) the ability to accept different shapes. A great improvement in future research will be the development of a multi-sensor array. Using more than one detector element will allow one to scan a certain area of the material faster than if one were to move only one element. Besides, by timing the electric outputs of elements, the array can be made sensitive in a certain direction with a listening focus at a particular depth. To improve resolution, dynamic focusing can be applied as well.[73] The axial (or depth) resolution of such detectors is determined by the ultrasound bandwidth of

the detector. The lateral resolution depends on the size of the source, i. e., the diameter of the transducer or the focal diameter of the ultrasonic or light beam. For a multi-sensor array the length of the array and the size of each element affects the lateral resolution as well.[32] It has been reported that ultrasonic images obtained at 200 MHz had a resolution of 6-7 μm, while 50 MHz could resolve about 50-100 μm.[74] Polymer transducer arrays used to be difficult to fabricate because it was difficult to cut the pieces. However, emerging technologies allow for etching an electrode pattern on the surface of the film or depositing the co-polymer directly onto silicon wafers. To avoid coupling among elements, the wafers are etched and the polymer is applied by spin coating and poling.[75]

7.2 Image Reconstruction

A 3-D image is desirable, therefore, applications of tomographic techniques are indicated. Optical and acoustical data will be acquired by both moving the laser source and focusing the light into different depths of the tooth. It has been suggested [76] that attenuation tomography and/or time-of-flight tomography is applied. Effects from secondary waves should be addressed due to propagation through nonlinear reactive media, or from multiple reflections.

The path of sound waves through different media is not necessary a straight path. Due to diffraction and reflections from boundaries, it can be deflected from its original direction, and moreover the signals may be delayed. Both the attenuation and the delay

of the signal can be measured to give information on the attenuation coefficient and the refraction index of the medium. Ideas for attenuation and refractive index tomography are presented below.

7.2.1 Attenuation Tomography

Let α(f) be the frequency dependent attenuation coefficient of an object. Using the energy-ratio method to measure the integrated attenuation we get:

$$\int_0^l \alpha(l,f)dl = -\frac{1}{2}ln\Big|\frac{E_1}{E_2}\Big|. \tag{7.2}$$

The weighted energies of the transfer functions of the tissue E_i with $i = 1, 2$ are given by:

$$E_i = 2\int_{f_1-\Omega}^{f_1+\Omega} |X(f-f_i)|^2 \Big|\frac{Y(f)}{Y_w(f)}\Big| df. \tag{7.3}$$

Here X(f) is an arbitrary weight function, Y(f) and $Y_w(f)$ are the Fourier transformed functions of the received signals from the material of interest and water, respectively.[77]

7.2.2 Refractive Index Tomography

The ultrasonic refractive index tomography uses the time delay of the sound waves, also called time-of-flight. Consider two layers of material and a primary acoustic wave P(f). The signal right before the boundary of the two layers can be expressed as:

$$Y_1(f) \quad = \quad P(f)\exp[-(\alpha_1 + i\beta_1)l_1]H_1(f)H_2(f), \tag{7.4}$$

$$Y_2(f) \quad = \quad A_\tau Y_1 \exp[-\int_0^l (\alpha_2 + i\beta_2)dx]. \tag{7.5}$$

In these equations $\alpha_i(f), i = 1, 2$ is the frequency dependent attenuation coefficient, $\beta_i(f) = 2\pi/V_i(x)$ is the frequency dependent phase coefficient of the material, A_τ is the attenuation due to differences in the impedance of both media (transmittance), and V(x) is the sound velocity at position x. H_1 and H_2 are the transfer functions of the transmitter and the receiver, respectively. These relations lead to an expression for the time delay as a function of the refractive index $n(x) = V_1(x)/V(x)$ as follows:

$$T_d = \frac{1}{V_1} \int_0^l (n(x) - 1)dx. \tag{7.6}$$

This expression is then used to retrieve the refractive index using Fourier backprojection algorithm described below. [76, 78]

7.2.3 Backprojection Algorithm

The backprojection algorithm is the subsequent application of Fourier slice theorem at different scan angles. As we are interested in a function f(x,y) describing the object, and having available results of several parallel scans with projections $P_\theta(t)$, the Fourier slice theorem can be written as:

$$F(u, \theta) = \int_{-\infty}^{\infty} \Big[\int_{-\infty}^{\infty} f(x, y)dy \Big] \exp[-\imath 2\pi ux]dx = \int_{-\infty}^{\infty} P_\theta(x) \exp[-\imath 2\pi ux]dx \tag{7.7}$$

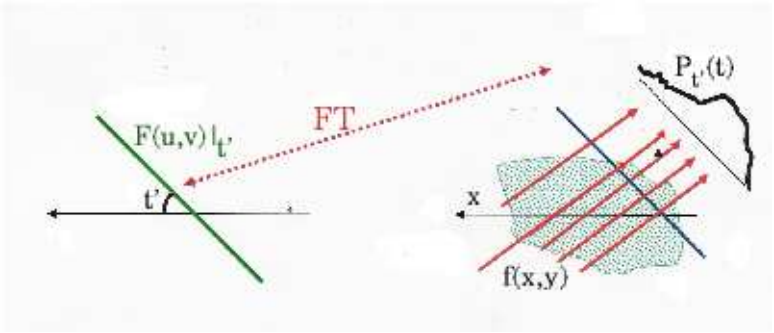

Figure 7.2: Illustration of the Fourier slice theorem

or

$$F(u, \theta) = FP_{\theta}(x). \tag{7.8}$$

The Fourier Slice theorem shows that the Fourier transform of a projection function can be used to find the Fourier transform of f(x,y) along a line in the two dimensional frequency domain (see Fig 7.2). The above methods for rendering 3-D image should be evaluated for optimum implementation for the envisioned instrument.

In conclusion, the presented work shows that imaging of dental tissue using photo-acoustics appears practical for applications in dental offices.

Bibliography

Bibliography

[1] A. R. Ten Cate. *Oral histology: development, structure, and function*. Mosby-Year Book, Inc., fifth edition.

[2] www.drkoop.com/imagepages/1121.htm.

[3] J. R. Zijp and J. J. Ten Bosch. Theoretical model for the scattering of light by dentin and comparison with measurements. *Appl. Opt.*, 32(4):411–415, 1993.

[4] V. M. Zolotarev and V. N. Grisimov. Architectronics and optical properties of dentin and dental enamel. *Opt. Spectr.*, 90(5):753–759, 2001.

[5] J. H. Kinney, J. Oliviera, D. L. Haupt, G. W. Marshall, and S. J. Marshall. The spacial arrangement of tubules in human dentin. *J. Mat. Sci.: Mat. Med.*, 12, 2001.

[6] G. Duplain, R. Boulay, and P. A. Belanger. Complex index of refraction of dental enamel at CO_2 laser wavelengths. *Appl. Opt.*, 26(20):4447–4451, 1987.

[7] D. Spitzer and J. J. Ten Bosch. The absorption and scattering of light in bovine and human dental enamel. *Calc. Tiss. Res.*, 17:129–137, 1975.

[8] L. Nicolaides, C. Feng, A. Mandelis, and S. H. Abrams. Quantitative dental measurements by use of simultaneous frequency-domain laser infrared photothermal radiometry and luminiscence. *Appl. Opt.*, 41(4):768–777, 2002.

[9] R. A. J. Groenhuis. *Scattering and absorption of turbid materials, especially dental enamel*. PhD thesis, University of Groningen, Groningen, The Netherlands, 1981.

[10] D. Fried, R. Glena, J. Featherstone, and W. Seka. Nature of light scattering in dental enamel and dentin at visible and near-infrared wavelengths. *Appl. Opt.*, 34(7):1278–1285, 1995.

[11] J. R. Zijp, J. J. Ten Bosch, and R. A. J. Groenhuis. HeNe-laser light scattering by human dental enamel. *J. Dent. Res.*, 74:1891–1898, 1995.

[12] J. J. Ten Bosch and J. R. Zijp. *Optical properties of dentin*, chapter Dentine and dentine reactions in the oral cavity, pages 59–65. IRL Press, Oxford, 1987.

[13] J. R. Zijp and J. J. Ten Bosch. HeNe-laser light scattering by bovine and human dentine. *Arch. Oral Biol.*, 36:283–289, 1991.

[14] F. E. Barber, S. Lees, and R. R. Lobene. Ultrasonic pulse-echo measurements in teeth. *Arch. Oral Biol.*, 14:745–760, 1969.

[15] S. R. Ghorayeb and T. Valle. Experimantal evaluation of human teeth using non-invasive ultrasound: echodentography. *IEEE UFFC*, 49(10):1437–1443, 2002.

[16] M. Culjat, R. S. Singh, D. C. Yoon, and E. R. Brown. Imaging of human tooth enamel using ultrasound. *IEEE T. Med. Imaging*, 22(4):526–529, 2003.

[17] R. G. Maev, L. A. Denisova, E. Y. Maeva, and A. A. Denissov. New data on histology and physico-mechanical properties of human tooth tissue obtained with acoustic microscopy. *Ultrasound Med. Biol.*, 28(1):131–136, 2002.

[18] J. H. Kinney, S. J. Marshall, and G. W. Marshall. The mechanical properties of human dentin: a critical review and re-evaluation of the dental literature. *Crit. Rev. Oral Biol. Med.*, 14(1):13–29, 2003.

[19] F. Povolo and E. B. Hermida. Measurement of the elastic modulus of dental pieces. *J. Alloy Compd*, 310:392–395, 2000.

[20] S. Habelitz, S. J. Marshall, G. W. Marshall, and M. Balooch. Mechanical properties of human dental enamel on the nanometre scale. *Arch. Oral Biol.*, 46:173–183, 2001.

[21] J. L. Cuy, A. B. Mann, K. J. Livi, M. F. Teaford, and T. P. Weihs. Nanoindentation mapping of the mechanical properties of human molar tooth enamel. *Arch. Oral Biol.*, 47:281–291, 2002.

[22] G. Willems, J. P. Celis, P. Lambrechts, M. Braem, and G. Vanherle. Hardness and young's modulus determined by nanoindentation technique of filler particles of dental restorativematerials compared with human enamel. *J. Biomed. Mater. Res.*, 27:747–755, 1993.

[23] S. Lees and F. R. Rollins. Anisotropy of hard dental tissue. *J. Biomech.*, 5:557–566, 1972.

[24] H. H. K. Xu, D. T. Smith, D. T. Jahanmir, E. Romberg, J. R. Kelly, V. P. Thompson, and E. D. Pekow. Indentation damage and mechanical properties of human enameland dentin. *J. Dent. Res.*, 77:472–480, 1998.

[25] J. H. Kinney, J. R. Gladden, G. W. Marshall, S. J. Marshall, J. H. So, and J. D. Maynard. Resonant ultrasound spectroscopy measurements of the elastic constants of human dentin. *J. Biomech*, 37:437–441, 2004.

[26] L. Angker, M. Swain, and N. Kilpatrick. Micro-mechanical characterisation of the properties of primary tooth dentine. *J. Dent.*, 31:261–267, 2003.

[27] A. Ansaldi, V. Fierro, and Ayllon. Measurement of the elastic modulus of dental pieces. *Interceram*, 47, 1998.

[28] M. Staines, W. H. Robinson, and J. A. A. Hood. Spherical indentation of tooth enamel. *J. Mat. Sci.*, 16:2551–2556, 1981.

[29] I. R. Spears. A three dimensional finite element model of prismatic enamel: a reappraisal of the data on the young's modulus of enamel. *J. Dent. Res.*, 76(10):1690–1697, 1997.

[30] C. G. A. Hoelen, F. F. M. de Mul, R. Pongers, and A. Dekker. Three-dimensional photoacoustic imaging of blood vessels in tissue. *Opt. Lett.*, 23(8):648–650, 1998.

[31] C. G. Hoelen, R. G. M. Kolkman, M. Letteboer, R. Berendsen, and F. F. M. de Mul. Photoacoustic tissue scanning (PATS). In *SPIE Conference on Optical Tomography and Spectroscopy of Tissue III*, volume 3597, pages 336–343, 1999.

[32] A. A. Oraevski, V. A. Andreev, and A. A. Karabutov. Laser opto-acoustic imaging of the breast: detection of cancer angiogenesis. In *SPIE Conference on Optical Tomography and Spectroscopy of Tissue III*, volume 3597, pages 352–363, 1999.

[33] A. A. Oraevski, A. A. Karabutov, and E. B. Savateeva. Opto-acoustic imaging of oral cancer: feasibility studies in hamster model of squamous cell carcinoma. In *SPIE Conference on Optical Tomography and Spectroscopy of Tissue III*, volume 3597, pages 385–396, 1999.

[34] P. C. Beard and T. N. Mills. Characterization of *post mortem* arterial tissue using time-resolved photoacoustic spectroscopy at 436, 461 and 532 nm. *Phys. Med. Biol.*, 42:177–198, 1997.

[35] P. C. Beard and T. N. Mills. 2d line-scan photoacoustic imaging of absorbers in a scattering tissue. In *Proc. SPIE*, volume 4256, pages 34–42, 2001.

[36] R. G. Kolkman, E. Hondebrink, W. Steenbergen, and F. de Mul. *Invivo* photoacoustic imaging of blood vessels using an extreme-narrow aperture sensor. *IEEE J. Sel. Top. Quant.*, 9:343–346, 2003.

[37] J. A. Viator, B. Choi, M. Ambrose, J. Spanier, and S. J. Nelson. *invivo* port-wine stain depth determination with a photoacoustic probe. *Appl. Opt.*, 42(16):3215–3224, 2003.

[38] J. A. Viator, G. Au, G. Paltauf, S. Jacques, S. Prahl, H. Ren, Z. Chen, and J. S. Nelson. Clinical testing of a photoacoustic probe for port wine stain depth determination. *Lasers Surg. Med.*, 30:141–148, 2002.

[39] X. Wang, Y. Pang, G. Ku, X. Xie, G. Stoica, and L. Wang. Noninvasive laser-induced photoacoustic tomography for structural and functional *invivo* imaging of the brain. *Nat. Biotech.*, 21(7):803–806, 2003.

[40] A. G. Bell. Upon the production of sound by radiant energy. *Philosophy Mag. J. Sci.*, XI:510–528, 1880.

[41] W. Demtröder. *Laser specrtoscopy: basic concepts and instrumentation.* Springer-Verlag, second edition.

[42] R. Gupta. *Laser spectroscopy.* American Association of Physics Teachers, 1993.

[43] J. Serbin, T. Bauer, C. Fallnich, A. Kasenbacher, and Arnold W. Femtosecond lasers as novel tool in dental surgery. *Appl. Surf. Sci.*, 197-198, 2002.

[44] C. K. N. Patel and A. C. Tam. Pulsed optoacoustic spectroscopy of condensed matter. *Rev. Mod. Phys.*, 53(3):517–550, 1981.

[45] A. A Oraevski, S. L. Jacques, and F. K. Tittel. Determination of tissue optical properties by piezoelectric detection of laser-induced stress waves. In *SPIE Laser-Tissue Interaction IV*, volume 1882, pages 86–101, 1993.

[46] T. van Leeuwen, E. Jansen, M. Motamedi, C. Borst, and A.Welch. *Optical-thermal response of laser-irradiated tissue*, chapter 21, pages 709–763. Plenum Press, New York, 1995.

[47] B. Choi and A. Welch. Analysis of thermal relaxation during laser irradiation of tissue. *Lasers Surg. Med.*, 29:351–359, 2001.

[48] M. W. Sigrist. Laser generation of acoustic waves in liquids and gases. *J. Appl. Phys.*, 60(7):R83–R121, 1986.

[49] A. L. McKenzie. Physics of thermal processes in laser-tissue interaction. *Phys. Med. Biol.*, 35(9):1175–1209, 1990.

[50] R. Birngruber. *Lasers Biol. Med.*, chapter Thermal modeling in biological tissues. New York: Plenum, 1980.

[51] A. C. Tam. Applications of photoacoustic techniques. *Rev. Mod. Phys.*, 58(2):381–431, 1986.

[52] A. Rosencwaig and A. Gersho. Theory of photoacoustic effect with solids. *J. Appl. Phys.*, 47(1):64–69, 1976.

[53] H. Vargas. Photoacoustic and related photothermal techniques. *Phys. Rep.*, 161(2):43–101, 1988.

[54] J.-M. Heritier. Electrostrictive limit and focusing effects in pulsed photoacoustic detection. *Opt. Comm.*, 44(4):267–272, 1983.

[55] H. M. Lai and K. Young. Theory of the pulsed optoacoustic technique. *J. Acoust. Soc. Am.*, 72(6):2000–2007, 1982.

[56] S. I. Anisimov, B. L. Kapeliovich, and T. L. Perelman. Electron emission from metal surfaces exposed to ultrashort laser pulses. *Sov. Phys.-JETP*, 39(2):375–377, 1974.

[57] E. G. Gamaly, B. Luther-Davis, and V. T. Tikhonchuk. Ablation of solids by femtosecond lasers: ablation mechanism and ablation thresholds for metals and dielectrics. *Phys. Plasmas*, 9(3):949–957, 2002.

[58] B. N. Chichkov, C. Momma, S. Nolte, F. von Albensleben, and A. T*ü*nnermann. Femtosecond, picosecond and nanosecond laser ablation in solids. *Appl. Phys. A*, 63:109–115, 1996.

[59] M. Frentzen and D. Hamrol. Kavit*ä*tenpr*ä*peration mit dem Er:YAG-laser-eine histologische studie. *Dtsch Zahnärztl*, Z 55, 2000.

[60] T. Q. Qiu and C. L. Tien. Size effects on nonequilibrium laser heating of metal films. *J. Heat Trans.*, 115:842–847, 1993.

[61] R. Schoenlein, W. Z. Lin, J. G. Fujimoto, and G. L. Eesley. Femtosecond studies of nonequilibrium electronic processes in metals. *Phys. Rev. Lett.*, 58(16):1680–1683, 1987.

[62] G. A. Korn and T. M. Korn. *Mathematical handbook for scientists and engineers: definitions, theorems, and formulas for reference and review.* McGrow-Hill, New York, 1968.

[63] M. H. Smith, R. L. Fork, and S. T. Cole. Safe delivery of optical power from space. *Opt. Exp.*, 8(10):537–546, 2001.

[64] C. Gerald and P. Wheatley. *Applied numerical analysis.* Addison-Wesley Publishing, Inc., 1989.

[65] E. H. Moriyama, R. A. Zangaro, P. D. C. Lobo, A. B. Villaverde, and M. T. Pacheco. Optothermal transfer simulation in laser-irradiated human dentin. *J. Biomed. Opt.*, 8(2):298–302, 2003.

[66] K. Nahen and A. Vogel. Investigations on acoustic on-line monitoring of IR laser ablation of burned skin. *Las. Surg. Med*, 25, 1999.

[67] W. H. Press, S. A. Teukolsky, W. T. Vetterling, and B. P. Flannery. *Numerical Recipes in Fortran: the Art of Scientific Computing.* Cambridge University Press, 2nd edition, 1992.

[68] W. Seka, D. Fried, J. D. B. Featherstone, and S. F. Borzillary. Light deposition in dental hard tissue and simulated thermal response. *J. Dent. Res.*, 74(4):1086–1092, 1995.

[69] F. Hirota and K. Furumoto. Temperature rise caused by laser (CO_2, Nd:YAG, Er:YAG) irradiation of teeth. *International Congress Series*, 1248:301–304, 2003.

[70] A. E. Siegman. *Lasers*. Mill Valley, Calif., 1986.

[71] R. Splinter. University of North Carolina at Charlotte. Private communications.

[72] M. Sato, I. Wakaki, Y. Watanabe, and N. Tanno. Fundamental characteristics of a synthesized light source for optical coherence tomography. *Appl. Opt.*, 44(13):2471–2481, 2005.

[73] F. W. Kremkau. *Diagnostic Ultrasound: Principles and Instruments*. W. B. Saunders Co, 5th edition, 1997.

[74] L. A. Denisova, R. G. Maev, I. V. Matveichuk, Y. I. Denisov-Nikolsky, A. A. Denissov, and E. Y. Maeva. New data on histology and physico-mechanical properties of human tooth tissue obtained with acoustic microscopy. In *Acoustic Imaging*, volume 26, pages 61–67, 2001.

[75] Measurement Specialties, Inc, 950 Forge Ave, Norristown, PA 19403. *Piezo film sensors techical manual*, 1999.

[76] K. Najarian. University of North Carolina at Charlotte. Private communications.

[77] A. C. Kak and M. Slaney. *Principles of Tomographic Imaging.* IEEE Press, 1998.

[78] C. Pintavirooj, A. Romputtal, A. Ngamlamiad, W. Withayachumnankul, and K. Hamamoto. Ultrasonic refractive index tomography. *J. WSCG*, 12(1-3):333–339, 2003.

Appendix

Source Code

The following FORTRAN source code is used to numerically evaluate the temperature distribution. The method includes Gear's method by using the IMSL library routine DMOLCH. The differential equations are defined in the subroutine FCNUT. The Delta distribution that describes the time component of the source function in the heat transfer equation is modeled as a very narrow Gaussian in the subroutine FCNUT as well. Typically, 1000 points are computed using a variable time-step, with the results put in a format ready to be plotted by the standard TECPLOT software package.

```
!       porcelain
        PROGRAM fsporsquare
        INTEGER LDY,NPDES,NX
        PARAMETER(NPDES=1,NX=321,LDY=NPDES)
        INTEGER I,IDO,J,NSTEP
        REAL*8 FCNUT,FCNBC,HINIT,T,TEND,TOL,
       &     XBREAK(NX),Y(LDY,NX)
        real*8 yinit,scale,tmax,tdummy,volsum,rdummy,radsum,r3sum
```

```
 integer icount,iflag,istart,ivol
 real*8 tau,pi,R1,rho,c,kappa,alphap,                                    10
&       lambda,w0,z,e,area,Jlas,a,z0
 common/parms/tau,pi,R1,rho,c,kappa,
&    alphap,lambda,w0,z,e,area,Jlas,a,z0
 INTRINSIC dble,float
 EXTERNAL FCNBC,FCNUT,DMOLCH,UMACH,WRRRN,
&         parmsdef
 callparmsdef
 yinit=300.d+00
 scale=1.d+00/dsqrt(2.D+00)*(1.d+00/20.d+00)
 open(35,file='xbreak.dat')                                              20
   do I=1,NX
     XBREAK(I)=(dble(I-161)*scale +5.d+00)*w0
     if (I.ge.140.and.I.le.161) write(35,*)I, XBREAK(I)
     Y(1,I)=yinit
   enddo
 close(35)
 TOL = 1.d-7
 HINIT = 0.d+00
 T     = 0.+00
```

```
      open(1,file='tst1d.dat')                                          30
      write(1,'(a)')' zone i=600 f=point'
     IDO  = 1
     NSTEP  = 1000
     icount= 0
     iflag  = 0
     istart= 0
     tmax =-1.d+00
     open(10,file='temp1.dat')
        do J=1,NSTEP
          TEND =FLOAT(J)*tau/10.                                        40
          icount=icount+1
            if(tend.ge.5.d+00*tau)then
               if(iflag.eq.0)then
                 istart=icount-1
                 iflag =1
               endif
             tend=float(j-istart+1)*1.d+00/100.d+00*
    &((a*a*w0*w0)/8.d+00)
            endif
          CALLDMOLCH(IDO,FCNUT,FCNBC,NPDES,T,TEND,NX,XBREAK,            50
```

```
&                TOL,HINIT,Y,LDY)
      write(1,'(1x,1d10.4,22(1p1d14.5))')T,
&     ((Y(1,i)−yinit),i=100,220,1)
       volsum=0.d+00
      doivol=1,nx
       volsum=volsum+((Y(1,ivol)−yinit))*scale
      enddo
       if(j.eq.141)then !81
          write(*,*)'XBREAK(',j,')=',XBREAK(j)
          open(11,file='rtemp9.dat')                                    60
            write(11,'(a)')' zone i=321 f=point'
            radsum=0.d+00
            r3sum=0.d+00
            doivol=1,nx
              rdummy=((Y(1,ivol)−yinit))
              radsum=radsum+rdummy
              r3sum=r3sum+(rdummy)**2
              write(11,*)(dble(ivol−161)*scale +5.d+00)*w0,rdummy
            enddo
            write(*,*)radsum,r3sum, radsum/r3sum                        70
          close(11)
```

```
            endif
!           161 − center; 141 − at r=w0
            tdummy=((Y(1,161)−yinit))
            if(tmax.lt.tdummy)tmax=tdummy
            write(10,'(1x,1d10.4,1p1d14.5)')T,tdummy
          enddo
        close(1)
        close(10)
        IDO = 3                                                          80
        CALLDMOLCH(IDO,FCNUT,FCNBC,NPDES,T,TEND,NX,XBREAK,TOL,
       &           HINIT,Y,LDY)
        open(10,file='temp1.dat')
        open(11,file='temp1sca2.dat')
 1      read(10,*,end=2)t,tdummy
        write(11,*)t,tdummy**2*radsum/r3sum*2.*pi !*4.d+00*pi/3.d+00
        goto1
 2      close(10)
        close(11)
        END                                                              90

        SUBROUTINEFCNUT(NPDES,X,T,U,UX,UXX,UT)
```

```
      INTEGER NPDES
      REAL*8 X,T,U(1),UX(1),UXX(1),UT(1)
      real*8 S,wz
      real*8 tau,pi,R1,rho,c,kappa,alphap,
     &       lambda,w0,z,e,area,J,a,z0
      common/parms/tau,pi,R1,rho,c,kappa,
     &    alphap,lambda,w0,z,e,area,J,a,z0
      wz=w0     !*dsqrt(1.d+00+(lambda*(z-z0)/pi/w0**2)**2)                  100
      S = 1.d+00/(rho*c)*J*2.d+00*
     &    dexp(-2.d+00*(x-5.d+00*w0)**2/w0**2*(w0/wz)**2)*
     &    dexp(-2.d+00*(T-1.5d+00*tau)**2/tau**2)/dsqrt(pi)*
     &    dsqrt(2.d+00)/tau
!       UT(1)=kappa/(rho*c)*UXX(1) + S
      UT(1)=kappa/(rho*c)*(1/X*UX(1)+UXX(1)) + S
      RETURN
      END

      SUBROUTINEFCNBC(NPDES,X,T,ALPHA,BETA,GAMP)                            110
      INTEGER NPDES
      REAL*8 X,T,ALPHA(1),BETA(1),GAMP(1)
        ALPHA(1) = 1.0d+00
```

```
      BETA(1) = 0.0d+00
      GAMP(1) = 0.0d+00
      RETURN
      END

      subroutineparmsdef
      real*8 tau,pi,R1,rho,c,kappa,alphap,                              120
     &  lambda,w0,z,e,area,J,a,taulas,z0
      real*8 alpha,z1,alphad,z2
      common/parms/tau,pi,R1,rho,c,kappa,
     &  alphap,lambda,w0,z,e,area,J,a,z0
      taulas=70.d-15          !s laser pulse width
      pi    =dacos(-1.d+00)
      R1    =0.004d+00
      rho   =2.4              !g/cm^3
      c     =1.1              !J/g.K
      kappa =9.99d-3          !W/cm.K                                   130
      alphap=1.d0             !cm^-1
      lambda=840.*1.d-07      !cm
      w0    =0.1d0            !cm beam radius
      z     =0.d+00
```

```
      e      =7.32d-9            !J energy per pulse
      area   =pi*w0*w0
      alpha  =1.d+00
      z1     =0.15d+00
      alphad=6.d+00
      z2     =0.1d+00                                                    140
      J      =(e/area*alphap)*
     &        (1-R1)*82.d6*0.04* !(laser freq)*(duration of gate opening)
     &        dexp(-alphap*z)    !*dexp(-alpha*z1)*dexp(-alphad*z2)
      a      =dsqrt(rho*c/kappa)
      z0     =0.d+00
      tau    =taulas!/a**2/w0**2*8.d+00
      return
      end
```

Vita

Pavlina Jetchkova Jeleva was born in November 26, 1974 in Shumen, Bulgaria. She graduated from the Mathematical High School in her hometown in 1991. During the first years in the University of Shumen she decided to continue her education specializing in the field of Biomedical Physics. She graduated with a Master of Science degree with a major in Medical Physics and Radioecology. In 1998 she became a fulltime student of the University of Tennessee Space Institute and in August 2001 she earned a Master of Science degree in Physics. Her work involved modeling multi-wavelength transmission in eye cataracts. She completed a Doctor of Philosophy degree in Physics in December 2005. Her research was in the area of the photo-acoustic dental imaging.